The Cryosphere

The influence of layering and barometric pumping on firn air transport in a 2-D model

Benjamin Birner[1], Christo Buizert[2], Till J. W. Wagner[3], and Jeffrey P. Severinghaus[1]

[1]Scripps Institution of Oceanography, University of California San Diego, La Jolla, CA 92093, USA
[2]College of Earth, Ocean and Atmospheric Sciences, Oregon State University, Corvallis, OR 97331, USA
[3]Department of Physics and Physical Oceanography, University of North Carolina at Wilmington, NC 28403, USA

Correspondence: Benjamin Birner (bbirner@ucsd.edu)

Abstract. Ancient air trapped in ice core bubbles has been paramount to developing our understanding of past climate and atmospheric composition. Before air bubbles become isolated in ice, the atmospheric signal is altered in the firn column by transport processes such as advection and diffusion. However, the influence of low-permeability layers and barometric pumping (driven by surface pressure variability) on firn air transport is not well understood and is not readily captured in conventional one-dimensional (1-D) firn air models. Here we present a two-dimensional (2-D) trace gas advection–diffusion–dispersion model that accounts for discontinuous horizontal layers of reduced permeability. We find that layering or barometric pumping individually yields too small a reduction in gravitational settling to match observations. In contrast, when both effects are active, the model's gravitational fractionation is suppressed as observed. Layering focuses airflows in certain regions in the 2-D model, which acts to amplify the dispersive mixing resulting from barometric pumping. Hence, the representation of both factors is needed to obtain a realistic emergence of the lock-in zone. In contrast to expectations, we find that the addition of barometric pumping in the layered 2-D model does not substantially change the differential kinetic fractionation of fast- and slow-diffusing trace gases. Like 1-D models, the 2-D model substantially underestimates the amount of differential kinetic fractionation seen in actual observations, suggesting that further subgrid-scale processes may be missing in the current generation of firn air transport models. However, we find robust scaling relationships between kinetic isotope fractionation of different noble gas isotope and elemental ratios. These relationships may be used to correct for kinetic frac-

tionation in future high-precision ice core studies and can amount to a bias of up to 0.45 °C in noble-gas-based mean ocean temperature reconstructions at WAIS Divide, Antarctica.

1 Introduction

In the upper 50–130 m of consolidated snow above an ice sheet, known as the firn layer, atmospheric gases gradually become entrapped in occluded pores and are eventually preserved as bubbles in the ice below. Antarctic ice core records containing these trapped gases have been critical in informing our understanding of the interplay of past climate and atmospheric trace gas variability over the past 800 000 years (Petit et al., 1999; Lüthi et al., 2008). As atmospheric gases migrate through the firn, they are modified in elemental composition and isotopic signature by several competing physical processes (Schwander et al., 1988, 1993; Trudinger et al., 1997; Buizert et al., 2012; Kawamura et al., 2013; Mitchell et al., 2015). Therefore, appropriate corrections must be applied to firn and ice core records to accurately reconstruct atmospheric trace gas histories.

Firn is a layered medium, in which the denser layers can impede vertical diffusion and transport (Hörhold et al., 2012; Mitchell et al., 2015; Orsi et al., 2015) (Fig. 1). The significance of these layers for firn gas transport remains unclear and motivates this work. Readers who are familiar with the structure of firn and its air transport processes may wish to skip ahead to the last paragraph of this section. To build some
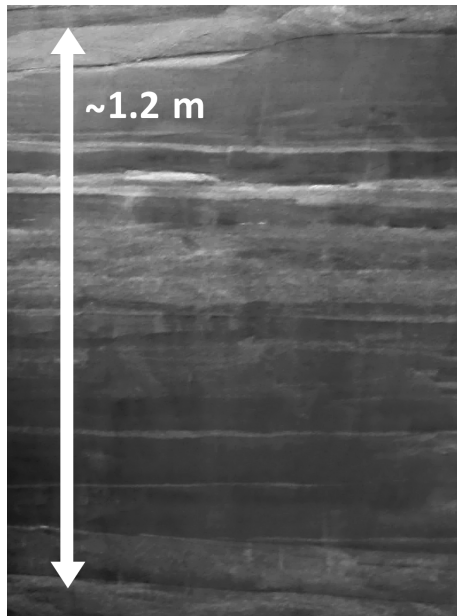
Figure 1. Layering of firn photographed in a surface pit at WAIS Divide. Image courtesy of Anaïs Orsi.

intuition about firn transport processes, a commonly used analytical model of firn air transport is provided in Appendix A.

Box 1| Porous media terminology

Porosity: the fraction of (firn) volume filled by gas

Permeability: the degree to which a porous medium permits viscous flow to pass through

Fickian diffusion: molecular diffusion that is proportional to the concentration gradient as described by Fick's first law

Tortuosity: measure of the twistedness of pathways through a porous medium

---

We distinguish four main processes affecting the composition of air in firn: diffusion, advection, dispersion, and convective mixing. Molecular diffusion, driven by concentration gradients in the firn, is the primary mode of horizontal and vertical transport. Molecular diffusion also enables gravitational fractionation, or "settling", of trace gases in proportion to their masses (Schwander, 1989; Sowers et al., 1989; Schwander et al., 1993; Trudinger et al., 1997). Gravitational settling leads to an enrichment of heavy isotopes with depth that is described in equilibrium by the barometric equation (Schwander, 1989; Sowers et al., 1989; Craig et al., 1988):

$$\delta_{\mathrm{grav}} = \left[\exp\left(\frac{g\,\Delta m}{R\,T} z \right) - 1 \right] \cdot 1000\%o, \qquad (1)$$

where $\delta \equiv \frac{r_{\mathrm{sample}}}{r_{\mathrm{standard}}} - 1 \equiv q - 1$, with r being the isotope ratio (unitless), z the depth (m), T the absolute temperature (K),
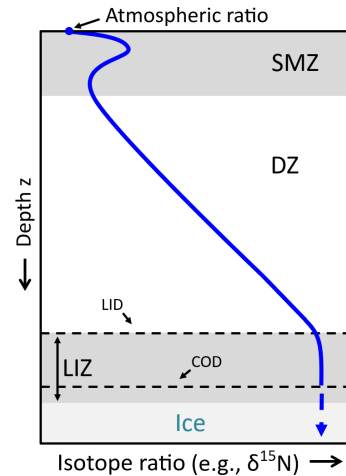

Figure 2. Schematic depiction of a typical isotope profile. The surface mixed zone (SMZ), the diffusive zone (DZ), the lock-in zone (LIZ), and the ice below are indicated by shading. Further indicated are the lock-in depth (LID) and the close-off depth (COD) (see text).

Δm the isotope mass difference (kg mol^{-1}), g the gravitational acceleration (m s^{-2}), and R the fundamental gas constant (J mol^{-1} K^{-1}).

Gradual accumulation of snow and air bubble trapping leads to a slow, downward advection of the enclosed air. The net air advection velocity is slower than the snow accumulation rate (yet still downward in an Eulerian framework) because compression of the porous firn medium produces a flow of air upward relative to the firn matrix (Rommelaere et al., 1997).

Buoyancy-driven convection and brief pressure anomalies associated with wind blowing over an irregular topography cause strong mixing between the near-surface firn and the unfractionated atmosphere, smoothing concentration gradients (Colbeck, 1989; Severinghaus et al., 2010; Kawamura et al., 2013). This mixing causes substantial deviations from the gravitational settling equilibrium (i.e., the solution to Eq. 1) and leads to varying degrees of kinetic isotope fractionation. This is because faster-diffusing isotopes more readily return to thermal–gravitational equilibrium by diffusion (Buizert et al., 2012; Kawamura et al., 2013).

Lastly, surface barometric pressure variability on longer timescales ($> 1\,\mathrm{h}$) drives air movement down to the firn-ice transition. Building on work by Schwander et al. (1988), Buizert and Severinghaus (2016) suggest that surface pressure variability may produce significant pressure gradients in the firn that induce airflow. Porous firn has a high tortuosity, i.e., two points are typically connected by strongly curved paths, and the deep firn also contains many cul-de-sacs (Buizert and Severinghaus, 2016, their Fig. 2). Airflow through such a medium produces mass-independent dispersive mixing. Dispersion in this context is an emergent macroscopic phenomenon that describes microscopic velocity de-

viations from Darcy's law of bulk fluid flow in different pores. This process may be accounted for by adding a dispersive mixing term to the advection–diffusion equation traditionally used for trace gas transport in firn (e.g., Buizert and Severinghaus, 2016).

Together, these four processes yield a firn column that is split into a surface mixed zone (SMZ, which has historically been labeled the convective zone), a diffusive zone (DZ), and a lock-in zone (LIZ) (Fig. 2). The close-off depth (COD) occurs where the air content becomes fixed and pressure in open pores increases above hydrostatic pressure. We prefer the term "surface mixed zone" over the more commonly used terminology "convective zone" to acknowledge the dual nature of mixing driven by convection and high-frequency pressure variability in this region. Large seasonal temperature gradients in the SMZ can lead to isotopic fractionation, which is only partially attenuated (Severinghaus et al., 2001, 2010; Kawamura et al., 2013). Molecular diffusion dominates in the DZ but effective firn diffusivity decreases with depth due to the increasing influence of tortuosity hindering diffusion. Throughout the DZ, gravitational settling leads to an enrichment of all isotopes heavier than air in proportion to their mass difference. The top of the LIZ, the somewhat poorly defined lock-in depth (LID) horizon, is commonly deduced from a rather sudden change in the slope of the δ^{15}N, CO_2, or CH_4 profiles. Gravitational enrichment of isotopes ceases in the LIZ and isotope ratios remain constant with depth. We term any such deviation from gravitational equilibrium "disequilibrium" (without implying that such a situation is not in steady state).

The physical mechanism responsible for the cessation of gravitational enrichment in the deep firn is still not fully understood. Since chlorofluorocarbons (CFCs) and other anthropogenic tracers have been detected in firn air measurements from the LIZ well below the depth expected from pure advection, it is clear that some amount of vertical transport by molecular diffusion or dispersion continues in the LIZ (Severinghaus et al., 2010; Buizert et al., 2012; Buizert and Severinghaus, 2016). However, no further gravitational settling of isotopes occurs in the LIZ as indicated by constant δ^{15}N values. Furthermore, the vertical transport in the LIZ appears to be at least to some degree dependent on mass and diffusivity since the faster-diffusing CH_4 advances further in the LIZ than the slower-diffusing gases CFC-113 or CO_2 (Buizert et al., 2012). Therefore, transport in the LIZ cannot be explained by either mass-indiscriminate dispersive mixing or molecular diffusion alone. Most current 1-D firn air models use a greatly reduced molecular diffusivity in the LIZ and simultaneously introduce a mass-independent mixing term tuned to match measured trace gas profiles (Buizert et al., 2012).

Here, we explore the possibility that non-fractionating trace gas mixing in deep firn may be explained by the combination of barometric pumping and discontinuous horizontal layers that have nominal diffusivity. High-density layers

are empirically linked to low vertical permeability, increasing the firn's tortuosity and forcing extensive horizontal transport. The influence of layering on firn gas transport is mostly untested in numerical models so far since previous firn air models were generally limited to one dimension. In particular, we will test two mechanisms by which density layering could influence isotope ratios in firn air: (i) layering may reduce gravitational settling of isotopes because vertical settling of isotopes is absent during horizontal transport along layers; (ii) layering may modulate the mass-independent dispersive mixing effect of barometric pumping. Our analyses will focus on two Antarctic high-accumulation sites, WAIS Divide and Law Dome DSSW20K (Trudinger et al., 2002; Battle et al., 2011).

2 Methods

2.1 Governing equation and firn properties

We model 2-D trace gas transport in firn by numerically solving the advection–diffusion–dispersion equation, known from hydrology (Freeze and Cherry, 1979), adapted to firn (following Schwander et al., 1993; Rommelaere et al., 1997; Trudinger et al., 1997; Severinghaus et al., 2010; Buizert et al., 2012; Kawamura et al., 2013; Buizert and Severinghaus, 2016):

$$\widetilde{s}\frac{\partial q}{\partial t} = \nabla \cdot \left[\widetilde{s}\mathbf{D}_\mathrm{m}\left(\nabla q - \frac{\Delta m\, \boldsymbol{g}}{R\,T}q + \Omega\frac{\partial T}{\partial z}q\hat{\boldsymbol{k}}\right) + \widetilde{s}\mathbf{D}_\mathrm{d}\nabla q \right] - (\widetilde{s}\boldsymbol{u})\cdot\nabla q, \tag{2}$$

with $q \equiv \delta + 1$ the ratio of any isotope to $^{28}N_2$ relative to a standard material, $\widetilde{s} \equiv s_\mathrm{op}\exp\left(\frac{\Delta m\,g}{R\,T}z\right)$ the pressure-corrected open porosity ($\mathrm{m^3\,m^{-3}}$), T temperature (K), Ω the thermal diffusion sensitivity ($\mathrm{K^{-1}}$), and $\boldsymbol{u}$ the advection velocity field ($\mathrm{m\,s^{-1}}$). $\mathbf{D}_\mathrm{m}$ and $\mathbf{D}_\mathrm{d}$ are the 2-D molecular diffusion and dispersion tensors ($\mathrm{m^2\,s^{-1}}$). ∇q is the concentration gradient and $\nabla\cdot$ denotes the 2-D divergence operator. From left to right, the terms of Eq. (2) represent the rate of change in concentration or isotope ratio, Fickian diffusion, gravitational fractionation, thermal fractionation, dispersive mixing, and advection. Since Eq. (2) is only valid for the binary diffusion of a trace gas into a major gas, ratios of any two isotopes of masses x and y are obtained by separately simulating the transport of each isotope into the major gas $^{28}N_2$ and using the relationship

$$q_{x/y} = \frac{q_{x/28}}{q_{y/28}} \tag{3}$$

to calculate the isotope ratios of interest (Severinghaus et al., 2010).

Isotope ratios are assumed to be constant at the surface (Dirichlet boundary) and reconstructions of atmospheric CO_2 and CH_4 concentrations over the last 200 years are used
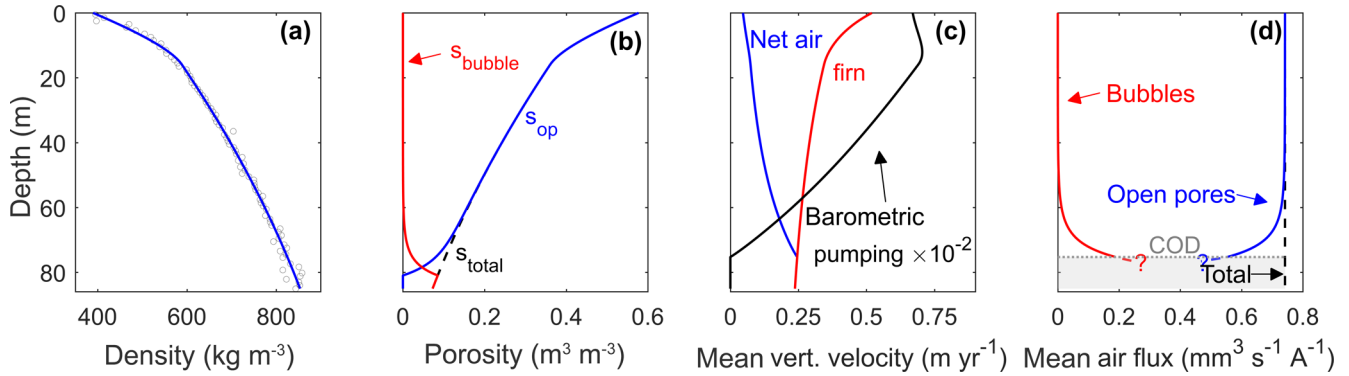
Figure 3. Firn conditions and modeled velocities profiles at WAIS Divide. **(a)** Density fit to observed data (data from Battle et al., 2011); **(b)** open, bubble (i.e., closed), and total porosity; **(c)** horizontally averaged barometric pumping velocity (i.e., time–mean horizontal average of $|\boldsymbol{u}_b|$, black), horizontally averaged net air velocity ($\overline{w}_{\text{firn}} + \overline{w}_r$, blue), and firn velocity ($\overline{w}_{\text{firn}}$, red); **(d)** mean air flux in open pores (blue) and bubbles (red).

to force runs of these anthropogenic tracers (see Supplement). The model time step is 3.5 days; smaller time steps have little impact on the model results and make the model impractical to run due to computational costs. The bottom boundary only allows for the advective flux to leave the domain (Neumann boundary). Diffusion and dispersive mixing cease below the COD. A periodic boundary condition is used in the horizontal direction. The horizontal extent of the model is varied between sites with differing snow accumulation rates to maintain a constant ratio of annual layer thickness to the model's spatial extent, which affects barometric pumping velocity. Firn density (Fig. 3a) is prescribed from a fit to the measured density profile at each site. Following Severinghaus et al. (2010) and Kawamura et al. (2013), empirical relationships are used to derive open and closed porosities from the density profile (Fig. 3b). The pressure-corrected open porosity $\widetilde{s}$ is assumed to be time independent.

2.2 Advection velocity and barometric pumping

The 2-D velocity field $\boldsymbol{u}$ is a result of a combination of (i) air migration with the firn ($\boldsymbol{w}_{\text{firn}}$), (ii) return flow of air from the firn to the atmosphere due to the gradual compression of pores ($\boldsymbol{u}_r$), and (iii) airflow resulting from barometric pumping ($\boldsymbol{u}_b$) (Figs. 3c, 4). $\boldsymbol{w}_{\text{firn}}$ is constrained by assuming a time-constant snow and ice mass flux at all depths. $\boldsymbol{u}_r$ is calculated based on the effective export flux of air in open and closed pores at the COD, imposing a constant mean vertical air flux throughout the firn column (Fig. 3d) (Rommelaere et al., 1997; Severinghaus and Battle, 2006). $\boldsymbol{u}_b$ is the airflow needed to re-establish hydrostatic balance in the firn in response to any surface pressure anomaly. Surface pressure variability is represented by (pseudo-) red noise, mimicking observed pressure variability at both sites. The near-coast location Law Dome is more strongly affected by storm activity than WAIS Divide with pressure variability $11.2\,\text{hPa}\,\text{day}^{-1}$ compared to $7\,\text{hP}\,\text{day}^{-1}$ at WAIS Divide. $\boldsymbol{u}_r$ and $\boldsymbol{u}_b$ follow
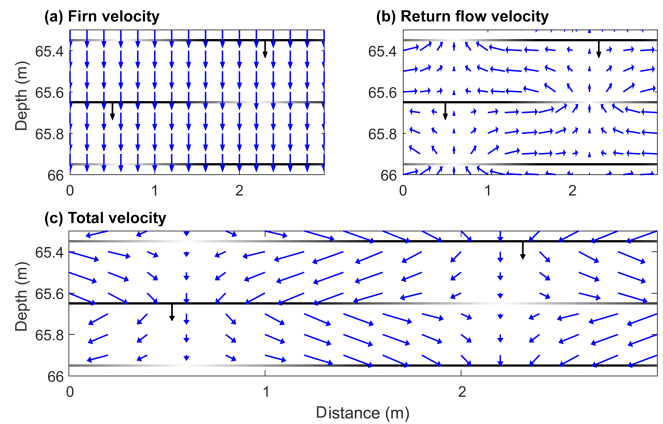

Figure 4. The different components of the velocity field: **(a)** firn velocity, **(b)** the velocity of air return flow to the atmosphere due to pore compression, and **(c)** net firn air advection velocity (a linear combination of the fields in panels **a** and **b**). Because of its alternating direction, barometric pumping yields no net flow but instantaneous flow field patterns look similar to panel **(b)**. Black arrows indicate the downward advection of layers at the firn velocity.

Darcy's law of flow through porous media (Darcy, 1856):

$$\boldsymbol{u} = -\frac{\kappa}{\widetilde{s}\mu}\nabla P, \tag{4}$$

with ∇P the pressure gradient, κ the permeability of firn, and μ the viscosity of air (Fig. 4). Further details on the derivation of these velocities are provided in the Supplement.

2.3 Firn layering

Idealized firn layering is implemented by forcing the vertical velocity components u_r and u_b, as well as all vertical diffusive fluxes between the grid boxes on either side of a layer to be zero. Only the advection of air with the firn ($\boldsymbol{w}_{\text{firn}}$) remains active at these grid box boundaries. Layering limits

vertical gas migration and yields almost exclusively horizontal transport between layers. We assign layers an infinitesimal thickness because of the computationally limited spatial resolution of the model. Layers are repeatedly introduced at a specific depth and migrate down with the velocity of the firn. The vertical distance between layers is set to correspond to the snow accumulation of 1 year and the horizontal extent of layers increases linearly with depth until they cover the entire domain at the COD. The mean layer opening size is held proportional to the annual layer thickness to make the vertical advection velocities independent of the arbitrary horizontal extent of the model. To obtain more realistic flow fields, the permeability of layers increases gradually towards both ends of a layer.

2.4 Dispersive mixing

The dispersion tensor $\mathbf{D}_d$ is made up of two components: (i) non-fractionating mixing of air in the SMZ and (ii) dispersive mixing caused by barometric pumping in the tortuous firn medium. First, the SMZ is commonly represented by mass-independent ("eddy") diffusion acting in the vertical and horizontal directions. The corresponding diffusivity profile $D_{SMZ}(z)$ is prescribed as an exponential decay away from the snow–atmosphere interface (Kawamura et al., 2013). Its maximum surface value and the decay constant are chosen to match observed $\delta^{15}N$ values in the deep firn. After reaching a specified maximum depth of 8 m at WAIS Divide and 14 m at Law Dome DSSW20K, D_{SMZ} tapers linearly to zero over the next 2 m.

Second, airflow through any dispersive medium leads to mixing in the directions longitudinal and transverse to the flow. Because barometric pumping velocities are orders of magnitude faster than the return flow, dispersive mixing is dominated by barometric pumping. The degree of dispersive mixing in firn presumably depends on the direction of flow and differs between the longitudinal-to-flow and transverse-to-flow direction. However, the treatment of anisotropic media is complex and only one parameterization for vertical, longitudinal-to-flow dispersion in firn is currently available (Buizert and Severinghaus, 2016). Therefore, we assume that the dispersivity α of firn is isotropic and linearly dependent on the magnitude of the flow velocity vector ($v \equiv |\boldsymbol{u}_b + \boldsymbol{u}_r|$). In this case, the 2-D dispersion tensor becomes

$$\mathbf{D}_d = (\alpha v + D_{SMZ})\,\mathbf{I}, \tag{5}$$

with $\mathbf{I}$ the second-order identity matrix (Freeze and Cherry, 1979; Buizert and Severinghaus, 2016). The dispersion flux term in Eq. (2) simplifies to

$$\widetilde{s}\mathbf{D}_d\nabla q = \widetilde{s}\,[\alpha v + D_{SMZ}]\,\nabla q. \tag{6}$$

The dispersivity parameterization of Buizert and Severinghaus (2016) is based on direct measurements of cylindrical firn samples from Siple Station, Antarctica, performed by Schwander et al. (1988). The parameterization relates dispersivity to open porosity s_{op} as

$$\alpha\left(s_{op}\right) = \widetilde{s}\left[1.26\exp\left(-25.7 s_{op}\right)\right]. \tag{7}$$

A factor of $\widetilde{s}$ was added to the original parameterization by Buizert and Severinghaus (2016) because α relates dispersive mixing to flow velocities per unit pore cross section (w_{pores}). Schwander et al. (1988), however, originally measured the considerably slower bulk airflow per unit firn cross section (i.e., $w_{bulk} = \frac{w_{pores}}{\widetilde{s}}$). Since dispersivity is a scale-dependent property, it is important to use parameterizations that are compatible with the resolution of the numerical model. The sample size of Schwander et al. (1988) (30 mm diameter and 50 mm length) approximately matches the resolution of our numerical model (30 × 40 mm) and thus should adequately approximate subgrid-scale (i.e., pore-scale) mixing processes that currently cannot be resolved. Spatial inhomogeneity of subgrid-scale firn dispersivity that was not captured by the sampling of Schwander et al. (1988) cannot be accounted for in the model. Dispersion on larger scales such as the interaction of flow and layers is explicitly represented in the model by the interplay of advection and diffusion. Thus, dispersive mixing is fully constrained in the model and based on empirical parameterizations that are not subject to tuning.

2.5 Molecular diffusion

The (effective) molecular diffusivity profile is established by simultaneously fitting the simulated CO_2 and CH_4 profile to real firn measurements at both sites. Effective vertical diffusivity decreases with depth to represent the subgrid-scale effect of decreasing pore connectivity and increasing firn tortuosity, which is not fully represented by the explicit macroscopic layers in our model (Fig. 5). Diffusivities for other trace gases are calculated by scaling the tuned CO_2 diffusivity by the free air diffusivity of each gas relative to CO_2 (Trudinger et al., 1997). The diffusivity tuning presents an underconstrained problem because horizontal and vertical molecular diffusivities are essentially free parameters. It is qualitatively evident from firn air sampling that horizontal connectivity or diffusivity is much higher than vertical diffusivity in deep firn, but no satisfactory quantification of this anisotropy is available. As a best guess estimate, we set horizontal molecular diffusivities equal to 10× the vertical diffusivity at the same depth. There are many degrees of freedom in tuning molecular diffusivities and our diffusivity parameterization is therefore not unique. However, sensitivity tests with equal horizontal and vertical diffusivity in the model (compensated by shorter horizontal layers) yield comparable results.
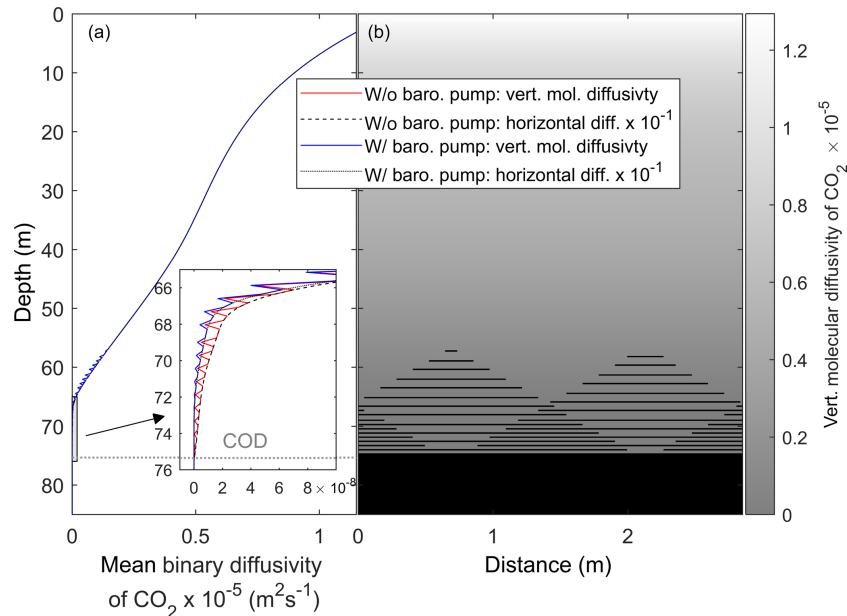
Figure 5. The CO_2 diffusivity profile at WAIS Divide. **(a)** Horizontally averaged, vertical and horizontal diffusivity in the model with and without barometric pumping. **(b)** Map of diffusivity in the 2-D model without barometric pumping. Only every third layer present in the model is shown here for clarity.

2.6 Thermal fractionation and temperature model

Finally, a 1-D vertical thermal model (Alley and Koci, 1990) is run separately to simulate the temperature evolution of the firn. The model is forced by a long-term surface temperature trend based on published records by Van Ommen et al. (1999), Dahl-Jensen et al. (1999), and Orsi et al. (2012). A mean Antarctic seasonal cycle derived from a 8–10-year climatology of automatic weather station observations at WAIS Divide and Law Dome (Lazzara et al., 2012) is superimposed on this trend. Horizontal temperature gradients in firn are small at both sites and neglected in this study.

Considerable temperature gradients can exist in present-day firn because of recent global atmospheric warming and these gradients can lead to increased isotope thermal fractionation, in particular of $\delta^{15}N$. The sensitivity of isotopes to diffuse in response to temperature gradients is captured by the thermal diffusion sensitivity Ω. The temperature dependence of Ω is approximated as a function of the effective average temperature T in Kelvin:

$$\Omega = \frac{a}{T} - \frac{b}{T^2},\tag{8}$$

or Ω is assumed to be temperature independent if the coefficients a and b are unknown for a specific isotope ratio (Severinghaus et al., 2001). Coefficients a and b were determined experimentally for different isotope ratios by Grachev and Severinghaus (2003a, b) and Kawamura et al. (2013).

A table of all model parameters and further details of the numerical realization of 2-D gas transport is provided in the Supplement.

3 Results

3.1 WAIS Divide

3.1.1 CO_2 and CH_4

A comparison of simulated and observed CO_2 and CH_4 profiles shows good agreement at WAIS (Fig. 6). In line with observations, both CO_2 and CH_4 concentrations decrease slowly with depth until ~ 68 m below the surface due to the gradually increasing gas age and the anthropogenic rise in atmospheric CO_2 and CH_4 concentrations. The more rapid decrease of CO_2 and CH_4 below ~ 68 m is explained by a much slower vertical penetration of air and a faster increase of the gas age with depth in the LIZ.

In the following discussion we will examine and compare results from four different versions of the 2-D model: with or without impermeable layers and with activated or deactivated barometric pumping. In versions without layering, our 2-D model loses all horizontal heterogeneity and will thus be referred to as a "1-D model" from here on. Since the explicitly implemented tortuosity from layering in the 2-D model affects molecular diffusion and dispersion equally it is represented by lowering the effective molecular diffusivity and dispersivity equally in the layered region of the 1-D version instead. Diffusivities are tuned such that the CO_2 pro-
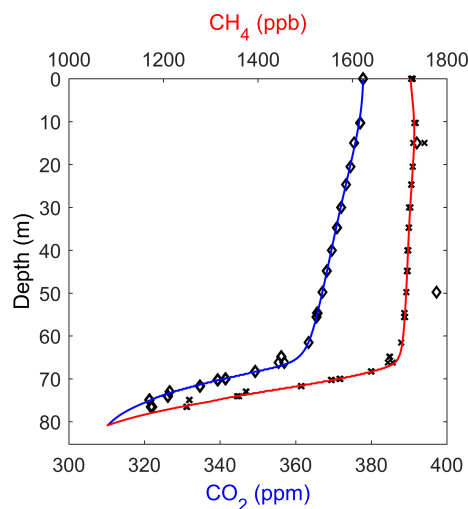
Figure 6. Simulated and observed CO_2 and CH_4 concentrations in the firn at WAIS Divide. The model is initialized with the recorded atmospheric trace gas concentrations in 1800 CE at all depths and is forced at the surface with histories of atmospheric CO_2 and CH_4 concentrations (Etheridge et al., 1996, 1998; Keeling et al., 2005; Buizert et al., 2012; Dlugokencky et al., 2016a, b). Markers indicate observed CO_2 (diamonds) and CH_4 (crosses) concentrations (Battle et al., 2011). Based on high CO_2 and CH_4, two samples at ~ 15 and ~ 50 m depth were likely compromised by modern air during analysis and are thus ignored in the curve fit. Differences in the CO_2 and CH_4 profiles between the 1-D model and the 2-D model with or without barometric pumping are not visible at the resolution of this figure but are illustrated in Fig. S12.

files are (nearly) identical. The small remaining deviations in CO_2 and CH_4 concentrations between model versions ($< \pm 0.4$ ppm and $< \pm 9$ ppb, respectively) are illustrated in Fig. S12.

3.1.2 δ^{15}N and thermal fractionation

In all four model setups, the seasonal cycle of temperature dominates the shape of the δ^{15}N profiles in the top ~ 30 m (Fig. 7). Warm summer temperatures drive the migration of heavy isotopes into the colder firn below and produce a δ^{15}N summer peak just below the surface (Severinghaus et al., 2001). In contrast, a minimum of δ^{15}N occurred in this region during the previous winter season when the thermal gradients were reversed. The remnants of this winter minimum are still visible in the gas record as anomalously low δ^{15}N values below the summer peak. The differences between observations and simulated δ^{15}N values in the top of the firn column are likely caused by the idealized representation of our seasonal cycle in the model.

3.1.3 Impact of reduced-permeability layers

In the layered 2-D model without barometric pumping, the simulated δ^{15}N values are close to observations at the top

of the LIZ but continue to increase with depth (Fig. 7). This is contradicted by observational data even when the unusually low δ^{15}N values at the COD and below are not taken into consideration (near the COD, firn air sampling becomes more difficult in the field and the potential for fractionation during sampling is increased). A closer inspection of the LIZ in Figs. 7 and 8 reveals a zigzag pattern in the δ^{15}N profile where impermeable layers are present. Simulated isotope ratios are higher just above horizontal layers, where heavy isotopes can accumulate, and are anomalously low below layers where heavy isotopes are more readily removed than supplied by gravitational settling. Gravitational settling through gaps in the layers sets up small horizontal concentration gradients that drive horizontal Fickian diffusion. Layering increases the effective travel path length for molecules and reduces the effective vertical diffusivity by increasing the tortuosity. However, layering alone appears to be insufficient to prevent gravitational settling completely, with continued gravitational enrichment being observed in the LIZ in this model version.

Is the impact of layers on the firn trace gas profile larger for isotopes such as δ^{15}N than for anthropogenic tracers such as CO_2, CFCs, or CH_4? All three gases have experienced large atmospheric variability in the industrial era. Therefore, the migration of these gases into the firn is dominated by vertical and horizontal Fickian diffusion. For δ^{15}N, in contrast, the effect of gravity is critical for transport. To answer the above question, we compare output from the layered 2-D model to the 1-D model without layers. We find that δ^{15}N values in the 1-D and 2-D model without barometric pumping are almost identical (Fig. 7). Layering in the 2-D model increases the effective transport distance for CO_2 just as much as for δ^{15}N and there is no disproportional impact of layering on gravitationally fractionated isotope ratios. Differences in explicitly represented tortuosity are automatically compensated in the 1-D model during tuning to the same CO_2 profile by reducing molecular diffusivities. Therefore, we conclude that layering alone does not simultaneously explain the observed CO_2 and δ^{15}N patterns.

3.1.4 Barometric pumping and the emergence of the LIZ

δ^{15}N values simulated by the 1-D and 2-D model with barometric pumping are lower in the LIZ than in both model versions without barometric pumping (Fig. 7). Accounting for barometric pumping improves the agreement with observations throughout the LIZ. However, the reduction of gravitational fractionation is substantially stronger when layers are present. Only when both layering and barometric pumping are accounted for in the model does the δ^{15}N profile correctly indicate no further gravitational enrichment in the LIZ and matches observations more closely. Dispersive mixing is nearly independent of molecular mass and does not lead to gravitational fractionation, but rather acts to elimi-
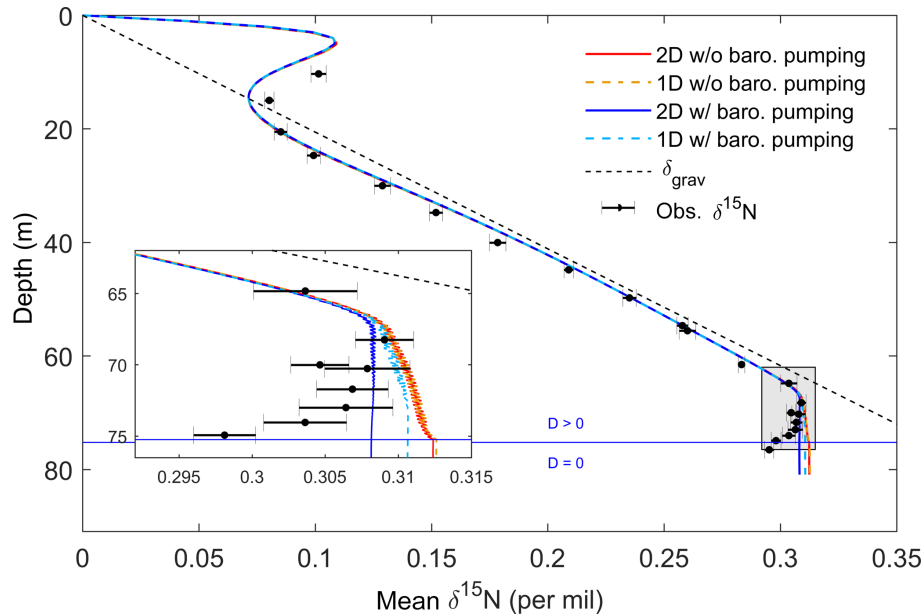
Figure 7. Horizontally averaged δ^{15}N at WAIS Divide. Model output is shown from four different versions of the 2-D model (see text). Black circles with error bars indicate the observed firn δ^{15}N (Battle et al., 2011). The dashed black line represents the equilibrium solution for pure gravitational settling (δ_{grav}). The horizontal blue line marks the depth where vertical diffusivity reaches zero. The inset shows a magnification of the lock-in zone.

nate the concentration gradients associated with gravitational settling. Although barometric pumping velocities are largest near the surface (Fig. 3c), significant dispersive mixing is generally limited to the LIZ because dispersivity of firn is inversely related to the open porosity in the parameterization of Buizert and Severinghaus (2016) and dispersion is overwhelmed by molecular diffusion in the DZ. Furthermore, molecular diffusivities drop rapidly in the LIZ in the model (Fig. 5). Because dispersion provides an additional transport mechanism for trace species, even less molecular diffusion is needed to match observed CO_2 and CH_4 concentrations in the LIZ when barometric pumping is active. Layering amplifies the importance of barometric pumping because gravitational fractionation between annual layers is restricted to the small gaps in the LIZ (Fig. 8). Narrow pathways amplify barometric pumping flow velocities and thus dispersive mixing in these regions (Fig. 4), thus overwhelming the influence of gravitational fractionation more readily than in the 1-D model. This effect is responsible for the larger differences between the δ^{15}N profiles obtained from the two model versions with barometric pumping in Fig. 7. The strength of dispersive mixing in our layered 2-D model is physically motivated; thus, barometric pumping and layering together lead to a more natural emergence of the δ^{15}N-defined LIZ in the 2-D model.
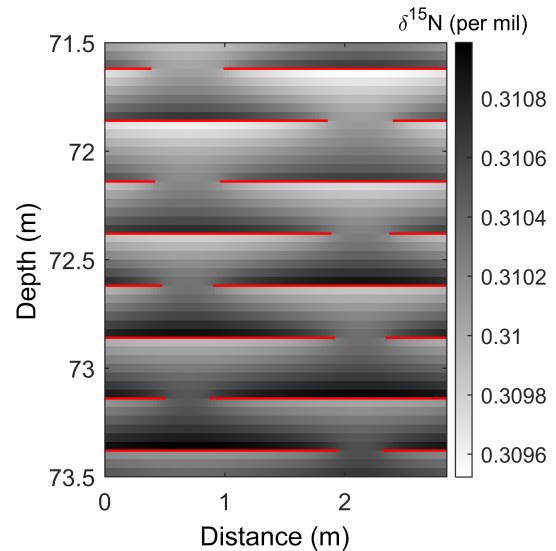

Figure 8. Simulated δ^{15}N in a section of the lock-in zone at WAIS Divide from the 2-D model not including barometric pumping. Impermeable horizontal layers are shown in red. The size of the openings in the layers shrink with increasing depth.

3.1.5 Surface mixed zone depth

We estimate the depth of the SMZ at WAIS Divide to be ~ 2.8 m. Multiple different procedures have been used to estimate SMZ thickness in the past, many of which rely on δ^{15}N data in the deep firn near the LIZ (Battle et al., 2011).

However, if the deep firn is affected by dispersive mixing due to barometric pumping, these estimates may be falsely attributing some fraction of the dispersive mixing in the deep firn to the SMZ. To address this problem, we follow the method of Severinghaus et al. (2001) in calculating SMZ thickness. This approach compares the depth where $\delta^{15}N$ reaches a certain value in two different model configurations with zero and non-zero values of D_{SMZ}. Thermal effects are neglected. The first setup is the 2-D model with barometric pumping as presented above but the dispersivity is set to zero everywhere without retuning the model. The SMZ thickness is calculated from the depth difference between this model run and a second model run where barometric pumping is deactivated and $D_{SMZ} = 0$. Thus only advection and gravitational fractionation shape the profile of $\delta^{15}N$. Our depth estimate of 2.8 m is within the 1.4–5.2 m range published previously (Battle et al., 2011).

3.2 Law Dome DSSW20K

At Law Dome DSSW20K, the firn thickness is ∼ 20 m less than at WAIS Divide. Accumulation rates are comparable, but annual-mean temperatures are ∼ 10 K warmer. The SMZ is slightly deeper and barometric pumping is stronger at Law Dome, yielding more near-surface and dispersive mixing. Constraining the SMZ depth at DSSW20K is more difficult because fewer $\delta^{15}N$ measurements are available for this site, and their associated uncertainty is, at ±15 per meg, much larger than at the more recently sampled WAIS Divide site (Trudinger et al., 2002). Molecular diffusion generally takes a less important role at DSSW20K and molecular diffusivities obtained by tuning are about half or less than those at WAIS Divide for most of the firn column. Thermal fractionation has a weaker impact on the isotope record near the surface at Law Dome due to the smaller amplitude of the seasonal cycle and stronger near-surface mixing compared to WAIS Divide. Figures of molecular diffusivity, advection velocities, and other firn properties at DSSW20K are provided in the Supplement.

Simultaneously matching the $\delta^{15}N$, CO_2, and CH_4 profile at Law Dome DSSW20K has proven difficult in the past (Trudinger et al., 2002; Buizert and Severinghaus, 2016). Simulated $\delta^{15}N$ in the LIZ is typically substantially higher than in observations. Buizert and Severinghaus (2016) suggested that barometric pumping in the deep firn may be able to reconcile this contradiction. However, the mixing obtained from theoretical predictions was insufficient to achieve a satisfactory fit. Buizert and Severinghaus (2016) hypothesized that firn layering may play a critical role in amplifying the impact of barometric pumping. The authors used an idealized eddy and molecular diffusivity profile in the deep firn to simulate the effect of layers on firn air transport. Using these diffusivity profiles, they were able to obtain good agreement with observed $\delta^{15}N$, CH_4, and $^{14}CO_2$. Our 2-D model includes an explicit representation of layering and is subject
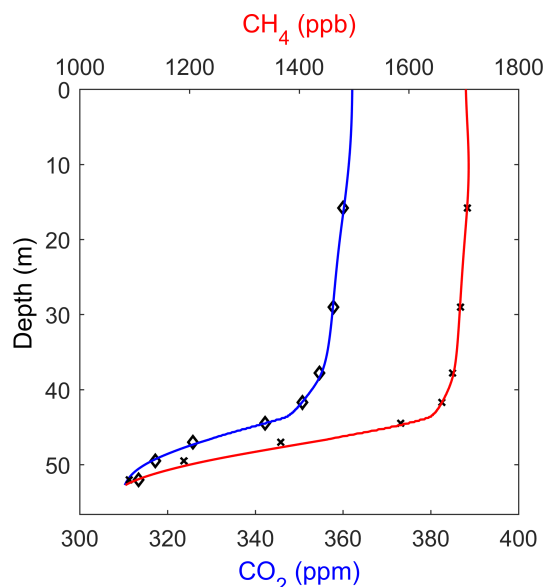

Figure 9. Simulated CO_2 and CH_4 concentrations in the firn at Law Dome DSSW20K. The model is forced with histories of atmospheric CO_2 and CH_4 concentrations from 1800 to 1998 CE (the date of sampling). Markers indicate observed CO_2 (diamonds) and CH_4 (crosses) concentrations (Trudinger et al., 2002).
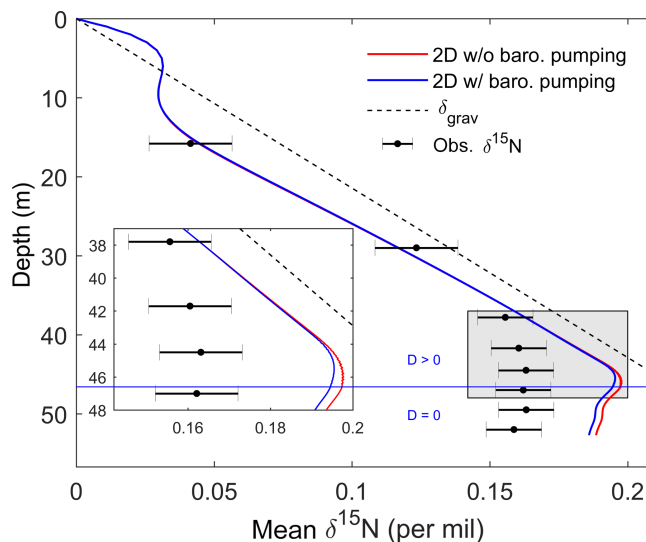

Figure 10. Horizontally averaged $\delta^{15}N$ at Law Dome DSSW20K. The solid lines show the results of the 2-D model (with layers) for the cases with (blue) and without (red) barometric pumping. Black circles with error bars indicate the observed firn $\delta^{15}N$ (Trudinger et al., 2002, 2013). The dashed black line represents the equilibrium solution for pure gravitational settling (δ_{grav}). The horizontal blue line marks the depth where vertical diffusivity reaches zero. The inset shows a magnification of the lock-in zone.

to similar physical constraints on barometric pumping as the 1-D model of Buizert and Severinghaus (2016). The model is tuned to optimize agreement with CO_2 and CH_4 and the
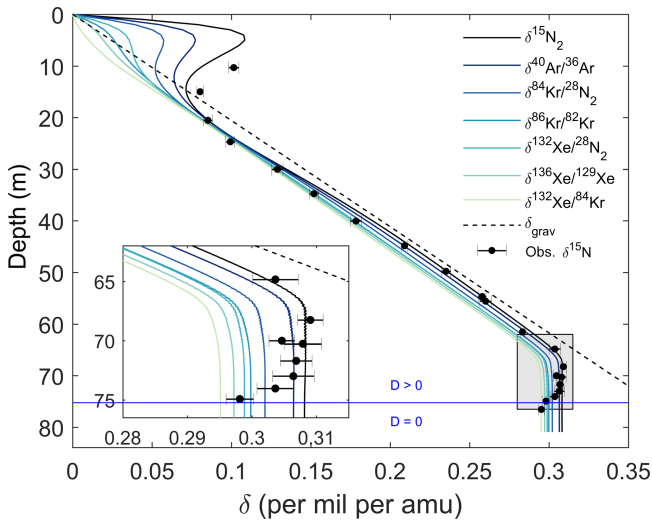
Figure 11. Horizontally averaged isotope ratios at WAIS Divide in the 2-D model including barometric pumping and horizontal layers. Isotope ratios are normalized to one atomic mass unit (amu) mass difference (Supplement). The dashed black line represents the equilibrium solution for pure gravitational settling (δ_{grav}). The horizontal blue line marks the depth where vertical diffusivity reaches zero. Observed δ^{15}N are shown as circles with horizontal error bars (Battle et al., 2011). The inset shows a magnification of the lock-in zone (gray patch).

Figure 12. Differential kinetic isotope fractionation (ϵ') profiles for different isotope pairs at WAIS Divide. Colored solid and dashed lines show results from the 2-D model with and without barometric pumping, respectively. ϵ' is defined as the (typically negative) difference between any mass-normalized isotope ratio and δ^{15}N (see text). Subscripts of one or two element names identify ratios as isotope or elemental ratios, respectively. The dashed black line highlights where molecular diffusivity in the model reaches zero.

patterns of both profiles are reproduced correctly (Fig. 9). But the disagreement between modeled and observed δ^{15}N in the deep firn remains despite barometric pumping producing substantial non-fractionating dispersive mixing in the region (Fig. 10). Simulated δ^{15}N values diverge from observations at ~ 38 m, where gravitational enrichment seems to stop in observations but continues in the model. In contrast, the LIZ, as defined by CO_2 and CH_4, only starts at roughly 43 m depth. Such an early onset of dispersive mixing is not supported by the dispersivity parameterization. However, only the longitudinal-to-flow mixing in the vertical direction at Siple Station was used to develop the firn dispersivity parameterization, and the use of this parameterization may be inappropriate at Law Dome DSSW20K (Buizert and Severinghaus, 2016). Moreover, dispersivity typically differs in the horizontal and vertical as well as the longitudinal-to-flow and the traverse-to-flow directions, an effect that is not accounted for in this study because of a lack of observational evidence to constrain anisotropic dispersivity.

4   Discussion

4.1   Differential kinetic isotope fractionation

Isotope ratios in firn typically do not reach values as high as predicted from gravitational equilibrium due to the influence of advection and non-fractionating dispersive mixing
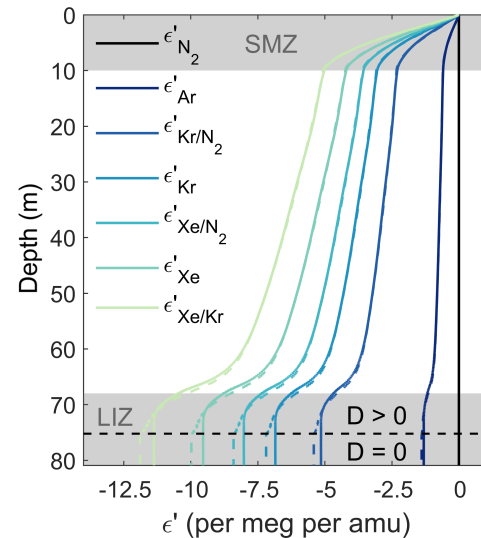
(Trudinger et al., 1997; Kawamura et al., 2013; Buizert and Severinghaus, 2016). Advection and mass-independent mixing transport less-fractionated air down in the firn column and act to counterbalance the enrichment of heavy isotopes by gravitational fractionation. As a result, all isotope ratios fall below the gravitational settling line δ_{grav} (Fig. 11) but the magnitude of the deviation depends on the specific isotope pair.

The magnitude of disequilibrium of different isotope and elemental ratios is quantified here by defining the (mass-normalized) kinetic fractionation ϵ' relative to δ^{15}N (following Kawamura et al., 2013) as

$$\epsilon'_{x/y} \equiv \frac{1}{1000 \cdot \Delta m_{x/y}} \ln\left(\frac{q_{x/28}}{q_{y/28}}\right) - \ln\left(q_{15_N}\right), \qquad (9)$$

where $\Delta m_{x/y}$ is the mass difference (in $\mathrm{mol\,kg^{-1}}$) of isotopes x and y. This definition is similar to the ^{86}Kr excess terminology introduced by Buizert and Severinghaus (2016) but ϵ' is given in the more precise $\ln(q)$ notation and uses δ^{15}N as reference instead of δ^{40}Ar / ^{36}Ar. To calculate $\epsilon'_{x/y}$, isotope ratios must have been previously corrected for the influence of thermal fractionation by removing temperature effects with a suitable firn air transport model (Fig. 12).

The degree of disequilibrium, represented by ϵ', is controlled by differential kinetic isotope fractionation. Heavy, slow-diffusing isotopes approach gravitational equilibrium more slowly than lighter, faster-diffusing isotopes. Therefore, slow-diffusing isotopes experience larger kinetic frac-
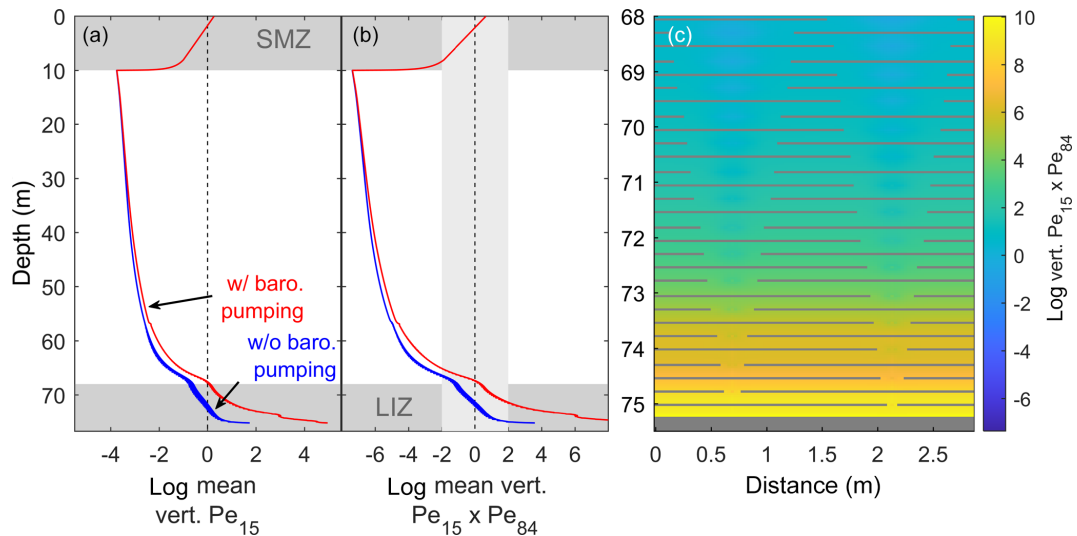
Figure 13. The balance of fractionating and non-fractionating mixing at WAIS Divide. Panel **(a)** illustrates the horizontally averaged modified Péclet number of δ^{15}N (Pe_{15}, see text). Blue and red lines show results from the 2-D models with and without barometric pumping. The strength of dispersive mixing in the calculations is given by the mean barometric pumping flow velocities at the site. Panel **(b)** displays the product of the modified Péclet numbers for δ^{15}N and ^{84}Kr / ^{28}N$_2$ (Pe_{84}). The region where ϵ' changes with depth should be greatest (i.e., where the product of the modified Péclet numbers is near 1) is highlighted by a gray bar. Panel **(c)** provides a magnified 2-D map of this Péclet number product in the LIZ.

tionation (i.e., deviations from gravitational equilibrium) in regimes with non-zero advection or dispersion. Consequently, ϵ' is more negative for heavier, slower-diffusing isotopes. On its own, this rule of thumb cannot fully explain the pattern of ratios containing two different elements, such as ^{132}Xe / ^{28}N$_2$. The magnitude of disequilibrium in such mixed-element ratios is further discussed in Appendix B.

In the DZ, ϵ' decreases almost linearly with depth, while within the SMZ and LIZ ϵ' changes much more rapidly. Where molecular diffusivity is zero, ϵ' remains constant. This pattern is explained by the relative importance of advection and dispersive mixing compared to molecular diffusion in different regions of the firn column. The Péclet number (Pe) traditionally quantifies the ratio of the advective to the diffusive transport and is here defined as the ratio of the diffusive to the advective timescale ($\tau_{D_{\mathrm{m}}}$ and τ_{adv}). We add the timescale of dispersive mixing ($\tau_{D_{\mathrm{e}}}$) to the numerator because the effect of advection and dispersive mixing on the isotope profiles is very similar although the physics differ (Kawamura et al., 2013):

$$Pe \equiv \frac{\tau_{\mathrm{adv}} + \tau_{D_{\mathrm{e}}}}{\tau_{D_{\mathrm{m}}}} \sim \frac{\frac{W}{L} + \frac{D_{\mathrm{e}}}{L^2}}{\frac{D_{\mathrm{m}}}{L^2}} \sim \frac{W L + D_{\mathrm{e}}}{D_{\mathrm{m}}}, \qquad (10)$$

where $L = 1\,\mathrm{m}$ is the characteristic length scale of firn air transport and D_{m}, W, and D_{e} are characteristic values of the molecular diffusivity, the time mean vertical advection velocity, and the vertical dispersive or convective mixing at that depth.

This modified Péclet number varies in the model by several orders of magnitude through the firn column at WAIS Divide with peak values in the SMZ and the deep firn (Fig. 13). High modified Péclet numbers in the SMZ are caused primarily by large D_{e} values, and high modified Péclet numbers in the LIZ are mostly the result of low molecular diffusivities. Kawamura et al. (2013) showed analytically that relative kinetic isotope fractionation depends on the ratio of eddy diffusivity to molecular diffusivity, but the role of advection was neglected due to near-zero accumulation rates at the Megadunes site. The absolute difference in kinetic isotope fractionation (i.e., ϵ') should be greatest when the product of the modified Péclet numbers of both isotopes is near one. In line with these theoretical predictions, we observe almost no further isotopic enrichment of δ^{15}N in the LIZ when barometric pumping is included in the model and $Pe \gg 1$ (Figs. 7, 13). The largest changes of ϵ' occur in the 2-D model when the product of the modified Péclet numbers is within approximately 1–2 orders of magnitude of unity. This region is illustrated by the vertical gray bar in Fig. 13, which contains the SMZ as well as the beginning of the LIZ where non-fractionating mixing is of similar magnitude as molecular diffusion.

With active barometric pumping and centimeter-scale layering, the product of the modified Péclet numbers at the bottom of the LIZ becomes so large that ϵ' stops to decrease entirely in our model. If barometric pumping is neglected instead, the modified Péclet numbers in the layered 2-D model are considerably lower in the LIZ and some gravitational and kinetic fractionation persists (i.e., δ^{15}N and ϵ'

continue to change gradually). Therefore, barometric pumping leads to slightly weaker rather than stronger differential kinetic fractionation at the COD of WAIS Divide in the model, in contrast to expectations (Buizert and Severinghaus, 2016). Furthermore, layering and barometric pumping in the model seem to be insufficient to obtain the full ~ 5–23 per meg per amu range of ϵ'_{Kr} values measured in the WAIS Divide ice core record (WAIS Divide Project Members, 2015; Bereiter et al., 2018). Instead, other, unresolved (i.e., subgrid-scale) processes may be the reason for the large observed disequilibrium. Establishing a straightforward relationship between disequilibrium and surface pressure variability using firn air models alone may not be possible without more observational data.

4.2 Diffusive fractionation

Strong kinetic isotope fractionation can also be observed for trace gases that experience large changes in the atmospheric mixing ratio while the atmospheric isotope ratios remain constant (Trudinger et al., 1997; Buizert et al., 2013). As the concentration of a trace gas increases, isotopologues of the gas migrate into the firn column at different speeds because of small differences in their masses and diffusivities. This results in a relative depletion of the slower-diffusing isotopologue with depth called diffusive fractionation (Trudinger et al., 1997). During periods of abrupt CH_4 change, diffusive fractionation commonly amounts to a notable correction in ice core studies (Trudinger et al., 1997; Buizert et al., 2013). Diffusive fractionation of $\delta^{13}C$-CH_4 is strong and poorly constrained by models, to the degree that it prohibits the reliable atmospheric reconstruction of this parameter from firn air measurements (Sapart et al., 2013). Since diffusive fractionation is a type of kinetic fractionation, it can be tested in our model. We assume a constant atmospheric $^{13}C/^{12}C$ isotope ratio of 1.1147302 % for CO_2 (i.e., $\delta^{13}C$-$CO_2 = -8\,‰$) and 1.0709052 % for CH_4 (i.e., $\delta^{13}C$-$CH_4 = -47\,‰$). Thermal fractionation and gravitational settling are neglected to isolate the impact of the atmospheric mixing ratio change. The model including barometric pumping calculates $\delta^{13}C$-CO_2 and $\delta^{13}C$-CH_4 values depleted by up to ~ 0.2 and $\sim 2\,‰$ relative to the atmosphere in the WAIS Divide LIZ at the time of firn air sampling (Fig. 14). Without barometric pumping, delta values are notably higher because molecular diffusion is stronger, and the dispersive mixing no longer smooths out the profile in the deep firn.

4.3 Predicting disequilibrium

Past mean ocean temperature can be estimated from the noble gas concentrations in ice core bubbles (Headly and Severinghaus, 2007; Ritz et al., 2011; Bereiter et al., 2018). On glacial–interglacial timescales, atmospheric concentrations of noble gases are primarily controlled by gas dissolution in the ocean. Because the temperature sensitivity of
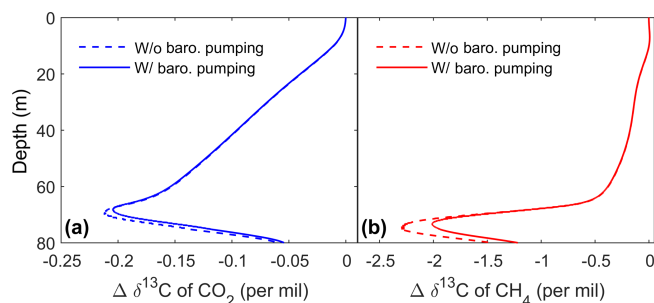

Figure 14. Diffusive fractionation effect at the time of sampling at WAIS Divide on $\delta^{13}C$ of **(a)** CO_2 and **(b)** CH_4. Atmospheric mixing ratios of $^{12}CO_2$, $^{13}CO_2$, $^{12}CH_4$, and $^{13}CH_4$ were obtained from atmospheric trace gas histories used to drive the firn air model (see Supplement) and assuming constant atmospheric isotope ratios of -8 and $-47\,‰$ for $\delta^{13}C$-CO_2 and $\delta^{13}C$-CH_4, respectively. Firn air values are presented as the difference from the constant atmospheric isotope ratios.

solubility is different for each gas, measurements of noble gas ratios in ice cores can be used to obtain a signal of integrated ocean temperature. However, as for any gas, the trace gas concentrations in bubbles must first be corrected for alterations of the atmospheric signal in the firn. In a recently published deglacial mean ocean temperature reconstruction, the WAIS Divide noble gas ice core record was corrected for gravitational fractionation and thermal fractionation using $\delta^{40}Ar/^{36}Ar$ measurements and a firn temperature gradient estimate (Bereiter et al., 2018). The authors further noted that different degrees of deviation from gravitational equilibrium (i.e., disequilibrium) can bias the gravitational fractionation correction applied to the raw noble gas record, which may lead to a cold bias of $\sim 0.3\,°C$ in Holocene and Last Glacial Maximum temperatures. Disequilibrium effects of -287.5 per meg for Kr/N_2, -833.3 per meg for Xe/N_2, and -545.7 per meg for Xe/Kr simulated by our model correspond to absolute temperature biases of 0.33, 0.41, and $0.45\,°C$, respectively, following the method of Bereiter et al. (2018). Because the magnitude of disequilibrium depends on firn properties and accumulation rate, glacial–interglacial changes in environmental boundary conditions may also affect the magnitude of disequilibrium in firn and thus the size of the relative deglacial temperature change estimated from noble gases.

In an attempt to compensate for disequilibrium effects and gravitational settling at the same time, it has been suggested that the elemental ratios Kr/N_2 and Xe/N_2 in bubbles should be corrected by subtracting krypton or xenon isotope ratios, respectively (Headly, 2008). This would assume that krypton and xenon isotopes may be influenced similarly by the processes responsible for creating disequilibrium in Kr/N_2 and Xe/N_2. Therefore, this approach may compensate for disequilibrium effects and gravitational settling simultaneously, but it has been untested in models so far. The

Table 1. ϵ' scaling factor in the 2-D model with barometric pumping between different element and isotope ratios from linear regression of ϵ' value pairs at all depths. $R^2 > 0.996$ for all relationships.

		Response: time-variable atmospheric gas ratios		
		ϵ'_{Kr/N_2}	$\epsilon'_{Xe/Kr}$	ϵ'_{Xe/N_2}
Predictor: isotope ratio	ϵ'_{Ar}	3.94	8.74	6.16
	ϵ'_{Kr}	0.75	1.66	1.17
	ϵ'_{Xe}	0.54	1.19	0.84

ϵ' values simulated here allow us to test this method quantitatively. We use a linear fit to predict ϵ'_{Kr/N_2} from ϵ'_{Kr}. The linear fit yields good agreement with the modeled ϵ'_{Kr} over the firn column ($R^2 > 0.998$), indicating that the scaling between ϵ' values is nearly independent of depth. We find that (mass-normalized) ϵ'_{Kr/N_2} should be approximately 75 % of (mass-normalized) ϵ'_{Kr} at the WAIS Divide site. Scaling relationships for other isotope and element pairs are shown in Table 1 and are equally robust. Moreover, our results show that the source of disequilibrium is irrelevant for the correction for the macroscopic processes represented in our model. Advection and convective or dispersive mixing all show the same scaling relationships for ϵ'. At Law Dome DSSW20K, the calculated ratio of ϵ'_{Kr/N_2} and ϵ'_{Kr} is at 75.9 % almost identical to the result at WAIS Divide. Sensitivity tests with the 1-D analytical model presented in Appendix A demonstrate that the disequilibrium scaling relationship between Kr isotopes and Kr / N$_2$ is robust to within ± 5 % over a wide parameter range of molecular diffusivity, eddy diffusivity, and advection velocity. Uncertainties become largest in the extreme case when ϵ'_{Ar}, the lowest simulated ϵ' value, is used to predict $\epsilon'_{Xe/Kr}$, the highest simulated ϵ' value, but they never exceed ± 25 %.

This suggests that the same scaling relationship between ϵ'_{Kr/N_2} and ϵ'_{Kr} may be assumed to hold for any ice core site without introducing large biases. ϵ'_{Kr} and ϵ'_{Xe} from combined measurements of $\delta^{15}N$, $\delta^{86}Kr / ^{82}Kr$, and $\delta^{136}Xe / ^{129}Xe$ in ice cores could be used to predict the disequilibrium effects on noble-gas elemental ratios (i.e., ϵ'_{Kr/N_2}, ϵ'_{Xe/N_2}, and $\epsilon'_{Xe/Kr}$) and allows us to make a gas-specific gravitational correction. Although predicted ϵ'_{Kr} values at WAIS Divide are close to the current analytical uncertainty of the $^{86}Kr / ^{82}Kr$ measurement, correcting for kinetic fractionation and disequilibrium will become advisable with future improvements in precision and may improve mean ocean temperature reconstructions.

5 Conclusions

We developed a two-dimensional firn air transport model that explicitly represents tortuosity in the firn column through migrating layers of reduced permeability. The idealized representation of firn layering is physically motivated and may illustrate the impact of firn density anomalies (i.e., summer vs. winter firn or wind crusts) on gas transport. The model also accounts for thermal fractionation, a surface mixed zone, and surface pressure-forced barometric pumping. Dispersive mixing as a result of barometric pumping is constrained in the model by previously published parameterizations and not subject to tuning. Simulations of the $\delta^{15}N$ profile at WAIS Divide show that extensive horizontal diffusion through the tortuous firn structure is required by the discontinuous layers. This limits the effective vertical diffusion of gases at depth. However, layering alone does not sufficiently reduce gravitational enrichment of isotopes in the deep firn. Similarly, the effect of barometric pumping alone is insufficient to obtain agreement with observations. The combination of barometric pumping with layering, in contrast, leads to amplified dispersive mixing. This is due to high velocity focusing in layer openings and leads to a more natural emergence of a lock-in zone in the model.

Previous studies have shown that downward advection, convective mixing, and dispersive mixing all hinder trace gases in reaching the isotope ratios expected from gravitational settling (e.g., Severinghaus et al., 2010; Kawamura et al., 2013; Buizert and Severinghaus, 2016). Kinetic fractionation is strongest for slow-diffusing gases and increases with firn column depth. Our numerical experiments show that barometric pumping leads to increased isotopic disequilibrium in the firn column. However, our simulations fail to account for the full range of ^{86}Kr excess observed in the WAIS Divide core, as well as for the relatively weak $\delta^{15}N$ enrichment seen at DSSW20K, suggesting that these effects are not caused by the presence of layering (as previously suggested) and that their origin must be sought elsewhere. We further find robust scaling relationships between the magnitude of disequilibrium in different noble gas isotope and elemental ratios. Our results suggest that, to first order, these scaling relationships are independent of depth in the firn column and independent of the cause of disequilibrium. Thus, a correction that accounts for differential kinetic fractionation may be applied to observed noble gas ratios in the reconstruction of mean ocean temperature.

Code availability. MATLAB code for the 2-D firn air transport model is available from the corresponding author on request.

Appendix A: An analytical solution for simplified firn air transport

Here, we seek an analytical solution to the following idealized scenario of firn air transport: firn air advection, diffusion, and dispersion in one dimension. In this case, vertical trace gas migration relative to the major gas nitrogen is governed by

$$\widetilde{s}\frac{\partial q}{\partial t} = \frac{\partial}{\partial z}\left[\widetilde{s}D_m\left(\frac{\partial q}{\partial z} - \frac{\Delta m\,g}{R\,T}q + \Omega\frac{\partial T}{\partial z}q\right) + \widetilde{s}D_e\frac{\partial q}{\partial z}\right] - \widetilde{s}w\frac{\partial q}{\partial z},$$
(A1)

with D_m and D_e the molecular and eddy diffusivity ($\mathrm{m^2\,s^{-1}}$) and w the effective vertical air advection velocity due to snow accumulation and pore compression ($\mathrm{m\,s^{-1}}$) (e.g., Schwander et al., 1993; Rommelaere et al., 1997; Trudinger et al., 1997; Severinghaus et al., 2010; Buizert et al., 2012; Kawamura et al., 2013). The five terms on the right-hand side of Eq. (A1) represent Fickian diffusion, gravitational settling, thermal fractionation, mass-independent dispersion, and gas advection (from left to right). A Dirichlet boundary condition is chosen at the top of the firn column and represents the well-mixed atmosphere (i.e., $q(0) \equiv 0$). The bottom boundary condition is given by a Neumann boundary condition, allowing only an advective flux to leave the domain ($\widetilde{s}\,(D_m + D_e)\frac{\partial q}{\partial z} - sD_m\left(\frac{\Delta m\,g}{R\,T} - \Omega\frac{\partial T}{\partial z}\right)q \equiv 0$ where $z = z\,(\text{COD})$).

Assuming steady state and neglecting changes of $\widetilde{s}$, D_m, D_e, and w with depth, Eq. (A1) reduces to (Severinghaus et al., 2010)

$$\frac{\partial q}{\partial t} = 0 = (D_m + D_e)\frac{\partial^2 q}{\partial z^2} - D_m(G - \mathcal{T})\frac{\partial q}{\partial z} - w\frac{\partial q}{\partial z}, \quad \text{(A2)}$$

where $G \equiv \frac{\Delta m\,g}{R\,T}$ and $\mathcal{T} \equiv \Omega\frac{\partial T}{\partial z}$ represent the constants in the gravitational and thermal fractionation term.

The solution to Eq. (A2) yields trace gas profiles above the COD in delta notation

$$\delta = \frac{\exp\left(\frac{D_m(G-\mathcal{T})+w}{D_m+D_e}z\right) - 1}{\frac{w}{D_m(G-\mathcal{T})}\exp\left(\frac{D_m(G-\mathcal{T})+w}{D_m+D_e}z_{\text{COD}}\right) + 1}, \quad \text{(A3)}$$

where $z_{\text{COD}} \equiv z\,(\text{COD})$ (Fig. S2). δ values below the COD are constant. Note that Eq. (A2) only applies to trace gas transport into N_2, not to transport of one trace gas into another trace gas, as discussed in the text. However, because $\delta^{15}N$ only requires calculating the transport of the trace gas $^{15}N^{14}N$ into the major gas $^{28}N_2$, the equation can be used as is to calculate $\delta^{15}N$.

By evaluating some extreme cases, Eq. (A3) illustrates a few key points about trace gas transport of $\delta^{15}N$ in firn. Under a large negative temperature gradient (i.e., atmospheric warming, $\mathcal{T} \to -\infty$), $\delta \to \infty$ and thermally sensitive gases are enriched in the firn because the numerator grows faster

than the denominator. Similarly, heavier gases ($G \to \infty$) are more strongly fractionated ($\delta \to \infty$) than lighter gases assuming they have the same molecular diffusivity. Advection ($w \to \infty$) and eddy mixing ($D_e \to \infty$) prevent the system from reaching the trace gas concentrations expected from gravitational settling and ultimately force concentrations to be constant ($\delta \to 0$). A lack of molecular diffusion ($D_m \to 0$) leads to the same result ($\delta \to 0$). Naturally, Eq. (A3) reduces to the profile of a gravitationally settled gas (i.e., Eq. 1) when $w \to 0$ and $D_e \to 0$.

Appendix B: Differential kinetic isotope fractionation in ratios of two different elements

Here we revisit the relative disequilibrium for ratios of two elements as seen in Figs. 11 and 12. First, recall the definition of ϵ' for a ratio of isotopes x and y (indicated by their nominal atomic masses, Eq. 9):

$$\epsilon'_{x/y} \equiv \frac{10^{-3}}{m_x - m_y}\ln\left(q_{x/y}\right) - \ln\left(q_{29/28}\right) = \ln\left(\frac{q_{x/y}^{\frac{10^{-3}}{m_x - m_y}}}{q_{29/28}}\right). \quad \text{(B1)}$$

Equation (3) shows that $q_{x/y}$ is the ratio of q values calculated for the transport of each isotope into $^{28}N_2$ ($q_{x/28}$ and $q_{y/28}$). $q_{x/28}$ (or $q_{y/28}$) may also be expressed in reference to nitrogen using the ϵ' value for the isotope

$$\frac{10^{-3}}{m_x - m_{28}}\ln\left(q_{x/28}\right) = \ln\left(q_{29/28}\right) + \epsilon_{x/28}'$$
$$\rightarrow \quad q_{x/28} = \left(q_{29/28}\cdot\exp\left(\epsilon_{x/28}'\right)\right)^{10^3\times(m_x - m_{28})}. \quad \text{(B2)}$$

Note that ϵ' by definition is already mass-normalized. It follows from Eqs. (3), (B1), and (B2) that

$$\epsilon'_{x/y} = \ln\left(\frac{\left(\frac{q_{x/28}}{q_{y/28}}\right)^{\frac{10^{-3}}{m_x - m_y}}}{q_{29/28}}\right)$$
$$= \ln\left(\frac{\left(\frac{(q_{29/28}\cdot\exp(\epsilon_{x/28}'))^{m_x - m_{28}}}{(q_{29/28}\cdot\exp(\epsilon_{y/28}'))^{m_y - m_{28}}}\right)^{\frac{1}{m_x - m_y}}}{q_{29/28}}\right). \quad \text{(B3)}$$

Equation (B3) may be rewritten to yield

$$\epsilon'_{x/y} = \frac{m_x - m_{28}}{m_x - m_y}\left[\ln\left(q_{29/28}\right) + \epsilon_{x/28}'\right]$$
$$- \frac{m_y - m_{28}}{m_x - m_y}\left[\ln\left(q_{29/28}\right) + \epsilon_{x/28}'\right] - \ln\left(q_{29/28}\right). \quad \text{(B4)}$$

Because the terms containing $q_{29/28}$ cancel, we obtain a straightforward expression to find ϵ' for any isotope ratio

from the ϵ' of two nuclides relative to $^{28}N_2$

$$\epsilon'_{x/y} = \frac{m_x - m_{28}}{m_x - m_y}\epsilon'_{x/28} - \frac{m_y - m_{28}}{m_x - m_y}\epsilon'_{y/28}. \qquad \text{(B5)}$$

Analysis of this relationship reveals that disequilibrium should most strongly affect ratios of two heavy isotopes, such as $^{132}Xe\,/\,^{84}Kr$, because heavy elements diffuse more slowly than N_2 (i.e., $\epsilon'_{x/28} \ll 0$) and the mass weighting factor is larger in the first than in the second term (i.e., $\frac{m_x - m_{28}}{m_x - m_y} \gg \frac{m_y - m_{28}}{m_x - m_y}$). Although this equation can theoretically predict ϵ' of any isotope ratio from ϵ' of the two isotopes x and y relative to $^{28}N_2$ (i.e., $\epsilon'_{x/28}$ and $\epsilon'_{y/28}$), in practice, this approach will not allow correcting for differential kinetic isotope fractionation. $\epsilon'_{x/28}$ cannot be measured directly and the atmospheric ratio of the noble gas x to nitrogen is not constant over long timescales. Thus, $\epsilon'_{x/28}$ will not only be affected by disequilibrium but will also be influenced by atmospheric variability resulting from gas specific solubility differences (i.e., precisely the mean ocean temperature signals we attempt to reconstruct). Instead we suggest that the scaling relationships provided in Sect. 4.3 can be used to predict the ϵ' of noble gas elemental ratios.

References

Alley, R. B. and Koci, B. R.: Recent warming in central Greenland?, Ann. Glaciol., 14, 6–8, 1990.

Battle, M. O., Severinghaus, J. P., Sofen, E. D., Plotkin, D., Orsi, A. J., Aydin, M., Montzka, S. A., Sowers, T., and Tans, P. P.: Controls on the movement and composition of firn air at the West Antarctic Ice Sheet Divide, Atmos. Chem. Phys., 11, 11007–11021, https://doi.org/10.5194/acp-11-11007-2011, 2011.

Bereiter, B., Shackleton, S., Baggenstos, D., Kawamura, K., and Severinghaus, J.: Mean global ocean temperatures during the last glacial transition, Nature, 553, 39–44, https://doi.org/10.1038/nature25152, 2018.

Buizert, C. and Severinghaus, J. P.: Dispersion in deep polar firn driven by synoptic-scale surface pressure variability, The Cryosphere, 10, 2099–2111, https://doi.org/10.5194/tc-10-2099-2016, 2016.

Buizert, C., Martinerie, P., Petrenko, V. V., Severinghaus, J. P., Trudinger, C. M., Witrant, E., Rosen, J. L., Orsi, A. J., Rubino, M., Etheridge, D. M., Steele, L. P., Hogan, C., Laube, J. C., Sturges, W. T., Levchenko, V. A., Smith, A. M., Levin, I., Conway, T. J., Dlugokencky, E. J., Lang, P. M., Kawamura, K., Jenk, T. M., White, J. W. C., Sowers, T., Schwander, J., and Blunier, T.: Gas transport in firn: multiple-tracer characterisation and model intercomparison for NEEM, Northern Greenland, Atmos. Chem. Phys., 12, 4259–4277, https://doi.org/10.5194/acp-12-4259-2012, 2012.

Buizert, C., Sowers, T., and Blunier, T.: Assessment of diffusive isotopic fractionation in polar firn, and application to ice core trace gas records, Earth Planet. Sci. Lett., 361, 110–119, https://doi.org/10.1016/j.epsl.2012.11.039, 2013.

Colbeck, S.: Air Movement in Snow due to Windpumping, J. Glaciol., 35, 209–213, 1989.

Craig, H., Horibe, Y., and T., S.: Gravitational separation of gases and isotopes in polar ice caps, Science, 242, 1675–1678, 1988.

Dahl-Jensen, D., Morgan, V. I., and Elcheikh, A.: Monte Carlo inverse modelling of the Law Dome (Antarc-

tica) temperature profile, Ann. Glaciol., 29, 145–150, https://doi.org/10.3189/172756499781821102, 1999.

Darcy, H.: Les Fontaines Publiques de la Ville de Dijon, Victor Dalmont, Paris, 1856.

Dlugokencky, E. J., Lang, P. M., Crotwell, A. M., Mund, J. W., Crotwell, M. J., and Thoning, K. W.: Atmospheric Methane Dry Air Mole Fractions from the NOAA ESRL Carbon Cycle Cooperative Global Air Sampling Network, 1983–2015, Version: 2016-07-07, 2016a.

Dlugokencky, E. J., Lang, P. M., Mund, J. W., Crotwell, A. M., Crotwell, M. J., and Thoning, K. W.: Atmospheric Carbon Dioxide Dry Air Mole Fractions from the NOAA ESRL Carbon Cycle Cooperative Global Air Sampling Network, 1968–2015, Version: 2016-08-30, 2016b.

Etheridge, D. M., Steele, L. P., Langenfelds, R. L., Francey, R. J., Barnola, J. M., and Morgan, V. I.: Natural and anthropogenic changes in atmospheric CO_2 over the last 1000 years from air in Antarctic ice and firn, J. Geophys. Res., 101, 4115–4128, https://doi.org/10.1029/95JD03410, 1996.

Etheridge, D. M., Steele, L. P., Francey, R. J., and Langenfelds, R. L.: Atmospheric methane between 1000 A.D. and present: Evidence of anthropogenic emissions and climatic variability, J. Geophys. Res., 103, 15979–15993, https://doi.org/10.1029/98JD00923, 1998.

Freeze, R. and Cherry, J.: Groundwater, Prentice-Hall, Inc., Englewood Cliffs, New Jersey, 1979.

Grachev, A. M. and Severinghaus, J. P.: Laboratory determination of thermal diffusion constants for $^{29}N_2 / ^{28}N_2$ in air at temperatures from -60 to $0\,°C$ for reconstruction of magnitudes of abrupt climate changes using the ice core fossil – air paleothermometer, Geochim. Cosmochim. Ac., 67, 345–360, 2003a.

Grachev, A. M. and Severinghaus, J. P.: Determining the Thermal Diffusion Factor for $^{40}Ar / ^{36}Ar$ in Air To Aid Paleoreconstruction of Abrupt Climate Change, J. Phys. Chem. A, 107, 4636–4642, https://doi.org/10.1021/jp027817u, 2003b.

Headly, M.: Krypton and xenon in air trapped in polar ice cores: paleo-atmospheric measurements for estimating past mean ocean temperature and summer snowmelt frequency, PhD dissertation, University of California, San Diego, 2008.

Headly, M. A. and Severinghaus, J. P.: A method to measure Kr/N2 ratios in air bubbles trapped in ice cores and its application in reconstructing past mean ocean temperature, J. Geophys. Res., 112, D19105, https://doi.org/10.1029/2006JD008317, 2007.

Hörhold, M. W., Laepple, T., Freitag, J., Bigler, M., Fischer, H., and Kipfstuhl, S.: On the impact of impurities on the densification of polar firn, Earth Planet. Sc. Lett., 325-326, 93–99, https://doi.org/10.1016/j.epsl.2011.12.022, 2012.

Kawamura, K., Severinghaus, J. P., Albert, M. R., Courville, Z. R., Fahnestock, M. A., Scambos, T., Shields, E., and Shuman, C. A.: Kinetic fractionation of gases by deep air convection in polar firn, Atmos. Chem. Phys., 13, 11141–11155, https://doi.org/10.5194/acp-13-11141-2013, 2013.

Keeling, C. D., Piper, S. C., Bacastow, R. B., Wahlen, M., Whorf, T. P., Heimann, M., and Meijer, H. A.: Atmospheric CO_2 and $^{13}CO_2$ Exchange with the Terrestrial Biosphere and Oceans from 1978 to 2000: Observations and Carbon Cycle Implications, in: A History of Atmospheric CO2 and Its Effects on Plants, Animals, and Ecosystems, edited by: Baldwin, I. T., Caldwell, M. M., Heldmaier, G., Jackson, R. B., Lange, O.

L., Mooney, H. A., Schulze, E.-D., Sommer, U., Ehleringer, J. R., Dearing, M. D., and Cerling, M. D., Springer, 83–113, https://doi.org/https://doi.org/10.1007/0-387-27048-5_5, 2005.

Lazzara, M. A., Weidner, G. A., Keller, L. M., Thom, J. E., and Cassano, J. J.: Antarctic Automatic Weather Station Program: 30 Years of Polar Observation, B. Am. Meteorol. Soc., 93, 1519–1537, https://doi.org/10.1175/BAMS-D-11-00015.1, 2012.

Lüthi, D., Le Floch, M., Bereiter, B., Blunier, T., Barnola, J.-M., Siegenthaler, U., Raynaud, D., Jouzel, J., Fischer, H., Kawamura, K., and Stocker, T. F.: High-resolution carbon dioxide concentration record 650,000–800,000 years before present, Nature, 453, 379–382, https://doi.org/10.1038/nature06949, 2008.

Mitchell, L. E., Buizert, C., Brook, E. J., Breton, D. J., Fegyveresi, J., Baggenstos, D., Orsi, A., Severinghaus, J., Alley, R. B., Albert, M., Rhodes, R. H., McConnell, J. R., Sigl, M., Maselli, O., Gregory, S., and Ahn, J.: Observing and modeling the influence of layering on bubble trapping in polar firn, J. Geophys. Res.-Atmos., 120, 2558–2574, https://doi.org/10.1002/2014JD022766, 2015.

Orsi, A. J., Cornuelle, B. D., and Severinghaus, J. P.: Little Ice Age cold interval in West Antarctica: Evidence from borehole temperature at the West Antarctic Ice Sheet (WAIS) Divide, Geophys. Res. Lett., 39, L09710, https://doi.org/10.1029/2012GL051260, 2012.

Orsi, A. J., Kawamura, K., Fegyveresi, J. M., Headly, M. A., Alley, R. B., and Severinghaus, J. P.: Differentiating bubble-free layers from Melt layers in ice cores using noble gases, J. Glaciol., 61, 585–594, https://doi.org/10.3189/2015JoG14J237, 2015.

Petit, R. J., Jouzel, J., Raynaud, D., Barkov, N. I., Barnola, J.-M., Basile, I., Bender, M., Chappellaz, J., Davis, M., Delaygue, G., Delmotte, M., Kotyakov, V. M., Legrand, M., Livenkov, V. Y., Lorius, C., Pépin, L., Ritz, C., Saltzman, E., and Stievenard, M.: Climate and atmospheric history of the past 420,000 years from the Vostok ice core, Antarctica, Nature, 399, 429–413, https://doi.org/10.1038/20859, 1999.

Ritz, S. P., Stocker, T. F., and Severinghaus, J. P.: Noble gases as proxies of mean ocean temperature: Sensitivity studies using a climate model of reduced complexity, Quaternary Sci. Rev., 30, 3728–3741, https://doi.org/10.1016/j.quascirev.2011.09.021, 2011.

Rommelaere, V., Arnaud, L., and Barnola, J.-M.: Reconstructing recent atmospheric trace gas concentrations from polar firn and bubbly ice data by inverse methods, J. Geophys. Res., 102, 30069–30083, 1997.

Sapart, C. J., Martinerie, P., Witrant, E., Chappellaz, J., van de Wal, R. S. W., Sperlich, P., van der Veen, C., Bernard, S., Sturges, W. T., Blunier, T., Schwander, J., Etheridge, D., and Röckmann, T.: Can the carbon isotopic composition of methane be reconstructed from multi-site firn air measurements?, Atmos. Chem. Phys., 13, 6993–7005, https://doi.org/10.5194/acp-13-6993-2013, 2013.

Schwander, J.: The transformation of snow to ice and the occlusion of gases, The Environmental Record in Glaciers and Ice Sheets, in: The Environmental Record in Glaciers and Ice Sheets, edited by: Oeschger, H. and Langway, C. C., John Wiley, 53–67, 1989.

Schwander, J., Stauffer, B., and Sigg, A.: Air mixing in firn and the age of the air at pore close-off, Ann. Glaciol., 10, 141–145, 1988.

Schwander, J., Barnola, J.-M., Andrié, C., Leuenberger, M., Ludin, A., Raynaud, D., and Stauffer, B.: The age of the air in the firn and the ice at Summit, Greenland, J. Geophys. Res., 98, 2831–2838, https://doi.org/10.1029/92JD02383, 1993.

Severinghaus, J. P. and Battle, M. O.: Fractionation of gases in polar ice during bubble close-off: New constraints from firn air Ne, Kr and Xe observations, Earth Planet. Sc. Lett., 244, 474–500, https://doi.org/10.1016/j.epsl.2006.01.032, 2006.

Severinghaus, J. P., Grachev, A., and Battle, M.: Thermal fractionation of airin polar firn by seasonal temperature gradients, Geochem. Geophy. Geosy., 2, 1–24, https://doi.org/10.1029/2000GC000146, 2001.

Severinghaus, J. P., Albert, M. R., Courville, Z. R., Fahnestock, M. A., Kawamura, K., Montzka, S. A., Mühle, J., Scambos, T. A., Shields, E., Shuman, C. A., Suwa, M., Tans, P., and Weiss, R. F.: Deep air convection in the firn at a zero-accumulation site, central Antarctica, Earth Planet. Sc. Lett., 293, 359–367, https://doi.org/10.1016/j.epsl.2010.03.003, 2010.

Sowers, T., Bender, M., and Raynaud, D.: Elemental and Isotopic Composition ofOccluded O2 and N2 in Polar Ice, J. Geophys. Res., 94, 5137–5150, https://doi.org/10.1029/JD094iD04p05137, 1989.

Trudinger, C. M., Enting, I. G., Etheridge, D. M., Francey, R. J., Levchenko, V. A., Steele, L. P., Raynaud, D., and Arnaud, L.: Modeling air movement and bubble trapping in firn, J. Geophys. Res., 102, 6747–6763, https://doi.org/10.1029/96JD03382, 1997.

Trudinger, C. M., Etheridge, D. M., Rayner, P. J., Enting, I. G., Sturrock, G. A., and Langenfelds, R. L.: Reconstructing atmospheric histories from measurements of air composition in firn, J. Geophys. Res., 107, 1–13, https://doi.org/10.1029/2002JD002545, 2002.

Trudinger, C. M., Enting, I. G., Rayner, P. J., Etheridge, D. M., Buizert, C., Rubino, M., Krummel, P. B., and Blunier, T.: How well do different tracers constrain the firn diffusivity profile?, Atmos. Chem. Phys., 13, 1485–1510, https://doi.org/10.5194/acp-13-1485-2013, 2013.

Van Ommen, T. D., Morgan, V. I., Jacka, T. H., Woon, S., and Elcheikh, A.: Near-surface temperatures in the Dome Summit South (Law Dome, East Antarctica) borehole, Ann. Glaciol., 29, 141–144, https://doi.org/10.3189/172756499781821382, 1999.

WAIS Divide Project Members: Precise interpolar phasing of abrupt climate change during the last ice age, Nature, 520, 661–665, https://doi.org/10.1038/nature14401, 2015.

Frieman Prize nomination for Benjamin Birner

To the selection committe,   19 April, 2019

This letter nominates a paper written by my PhD student Benjamin Birner for the
Frieman Prize. The paper's title is "The influence of layering and barometric pumping
on firn air transport in a 2-D model", and Mr. Birner is the first author. It was published
in June 2018 in The Cryosphere, and has four authors including myself. Mr. Birner
constructed the numerical model, created all of the analytical models, and performed
several simplified numerical simulations to rapidly test specific physical processes. The
original idea for the paper was mine, but I had very little involvement other than that.

Two other co-authors are Christo Buizert, a professor at Oregon State University who
provided advice to Mr. Birner about how to code the flow of air in a porous medium, and
Till Wagner, a former Scripps postdoc with Ian Eisenman who gave advice about
numerical solver schemes. In essence, these were technical contributions to the paper.

The primary creative input and exploration of the physics of isotope fractionation in the
firn (snow) in polar regions was done by Mr. Birner. He applied his strong physics
background to the problem with great passion and energy, and made several profound
breakthroughs. Most importantly, he was able to show that a two-dimensional model is
able to explain what prior 1-D models could not: namely that horizontal layering in snow
(due for example to episodic wind-packed layers that have very high density) can explain
why observed gravitational heavy-isotope settling typically ceases at about 70% of the
firn thickness. The curious feature in the bottom 30% of the firn is known as the "lock-in
zone", because it is the location where atmospheric gases are locked-in to the air bubbles
in ice and preserved.

All prior models of firn have had to artificially "terminate" vertical gas movement at the
top of the lock-in zone, a quite arbitrary and unphysical intervention. Mr. Birner's model
is the first to naturally simulate the emergent property of the lock-in zone, which is the
cessation of isotope fractionation. As such it is a first-order breakthrough, and I think a
highly appropriate choice for the Frieman Prize given Ed Frieman's physics orientation.

Sincerely,

Jeffrey P. Severinghaus
Professor of Geosciences and PI, Scripps Noble Gas Isotope Laboratory

Statement detailing each individual author's contribution to the paper

Jeff Severinghaus   Provided original idea to extend 1-D firn models to 2-D, with explicit representation of low-permeability layers with gaps allowing localized vertical airflow

Christo Buizert   Provided technical advice to Mr. Birner on coding airflow in a porous medium.

Till Wagner   Provided numerical solver techniques to Mr. Birner and advice on numerical schemes.

Benjamin Birner   Major creative input. Analyzed physics of turbulent and diffusive airflow, with goal of realistically simulating isotope fractionation and its cessation 70% of the way through the firn. Created several analytical models to explore exact solutions, for testing the accuracy of the numerical model and obtaining deeper insight of the physical processes at work in air movement in firn. Tested several alternative hypotheses using 1-D models and was able to falsify them. Created a very useful set of scaling relationships between isotopes and elemental ratios for studies of past mean ocean temperature, which require corrections of noble gas elemental ratios for disequilibrium. Successfully produced the first model that naturally simulates the "lock-in zone", as an emergent property of the layered nature of the snow.

The Cryosphere

Open Access

EGU

Supplement of

The influence of layering and barometric pumping on firn air transport in a 2-D model

B. Birner et al.

Correspondence to: Benjamin Birner (bbirner@ucsd.edu)

1   2D trace gas transport model

1.1   Numerical integration scheme

10   Trace gas migration in firn is governed by the following partial differential equation (Eq. (2) in main text)

$$\tilde{s}\frac{\partial q}{\partial t} = \nabla \cdot \left[\tilde{s}\mathbf{D}_m \left(\nabla q - \boldsymbol{G}\, q + \Omega \frac{\partial T}{\partial z} q\, \widehat{\boldsymbol{k}}\right)\right] + \nabla \cdot [\tilde{s}\mathbf{D}_d \nabla q] - (\tilde{s}\, \boldsymbol{u}) \cdot \nabla q \,, \tag{S1}$$

where $\boldsymbol{G} \equiv \frac{\Delta m\, \boldsymbol{g}}{R\,T}$, $q \equiv \frac{\delta}{1000} + 1$ is the trace gas or isotope mixing ratio, $\tilde{s} \equiv s_{op} \exp\left(\frac{M\,g}{R\,T}z\right)$ pressure-corrected open porosity ($\mathrm{m^3\,m^{-3}}$), T temperature (K), Δm isotope mass difference ($\mathrm{kg\,mol^{-1}}$) to the mass of air M ($\mathrm{kg\,mol^{-1}}$), $\boldsymbol{g}$ gravitational acceleration ($\mathrm{m\,s^{-2}}$), R the fundamental gas constant ($\mathrm{J\,mol^{-1}\,K^{-1}}$), $\boldsymbol{u}$ air advection velocity due to snow accumulation, pore compression and barometric pumping ($\mathrm{m\,s^{-1}}$), and Ω thermal diffusion sensitivity ($\mathrm{K^{-1}}$). $\mathbf{D}_m$ is the molecular diffusivity and $\mathbf{D}_d$ is the

15   dispersion tensor ($\mathrm{m^2\,s^{-1}}$). $\mathbf{D}_m$ has different entries on the diagonal to represent different strengths of molecular diffusion in the vertical and horizontal direction. Similarly, $\mathbf{D}_d$ is simplified to an "eddy diffusivity", $\mathbf{D}_e$, acting in vertical and horizontal direction as described in the text. $\tilde{s} = \tilde{s}(z)$, $T = \mathrm{T}(z, t)$, and $q = q(x, z, t)$ are scalar fields. Furthermore, $\boldsymbol{u} = u(x, z, t)\, \hat{\boldsymbol{\imath}} + w(x, z, t)\, \widehat{\boldsymbol{k}}$ is a vector field and $\nabla \equiv \frac{\partial}{\partial x}\hat{\boldsymbol{\imath}} + \frac{\partial}{\partial z}\widehat{\boldsymbol{k}}$ is the gradient operator in 2D.

Equation (S1) is discretized using a Crank-Nicolson time stepping scheme and central difference approximations derived

20   from flux balance on an Arakawa C (i.e., staggered; Fig. S1) grid as follows:

$$\tilde{s}(z)\frac{q(x, z, t + \Delta t) - q(x, z, t)}{\Delta t} = \frac{1}{2}\left[(\mathbf{A} + \mathbf{B})_{|t+\Delta t}\, q(x, z, t + \Delta t) + (\mathbf{A} + \mathbf{B})_{|t}\, q(x, z, t)\right], \tag{S2}$$

where

1

$$\mathbf{A}_{|t}\, q(x,z,t) \equiv \frac{-\tilde{s}u\left(x+\frac{\Delta x}{2},z,t\right)}{2\Delta x}\, q(x+\Delta x,z,t) + \frac{\tilde{s}u\left(x-\frac{\Delta x}{2},z,t\right)}{2\Delta x}\, q(x-\Delta x,z,t) - \frac{\tilde{s}w\left(x,z+\frac{\Delta z}{2},t\right)}{2\Delta z}\, q(x,z+\Delta z,t) +$$

$$\frac{\tilde{s}w\left(x,z-\frac{\Delta z}{2},t\right)}{2\Delta z}\, q(x,z-\Delta z,t) + \left[\frac{\tilde{s}u\left(x+\frac{\Delta x}{2},z,t\right)-\tilde{s}u\left(x-\frac{\Delta x}{2},z,t\right)}{2\Delta x} + \frac{\tilde{s}w\left(x,z+\frac{\Delta z}{2},t\right)-\tilde{s}w\left(x,z-\frac{\Delta z}{2},t\right)}{2\Delta z}\right] q(x,z,t)\,, \tag{S3}$$

$$\mathbf{B}_{|t}\, q(x,z,t) \equiv \frac{\tilde{s}D_h^*\left(x+\frac{\Delta x}{2},z,t\right)}{\Delta x^2} q(x+\Delta x,z,t) + \frac{\tilde{s}D_h^*\left(x-\frac{\Delta x}{2},z,t\right)}{\Delta x^2} q(x-\Delta x,z,t) + \left[\frac{\tilde{s}D_v^*\left(x,z+\frac{\Delta z}{2},t\right)}{\Delta z^2} - G\,\frac{\tilde{s}D_{m,v}\left(x,z+\frac{\Delta z}{2},t\right)}{2\Delta z} + \right.$$

$$\left. \frac{\tilde{s}D_{m,v}\Omega\left(x,z+\frac{\Delta z}{2}\right)\left(\frac{T(x,z+\Delta z,t)-T(x,z,t)}{\Delta z}\right)}{2\Delta z}\right] q(x,z+\Delta z,t) + \left[\frac{\tilde{s}D_v^*\left(x,z-\frac{\Delta z}{2},t\right)}{\Delta z^2} + G\,\frac{\tilde{s}D_{m,v}\left(x,z-\frac{\Delta z}{2},t\right)}{2\Delta z} - \right.$$

$$\left. \frac{\tilde{s}D_{m,v}\Omega\left(x,z-\frac{\Delta z}{2}\right)\left(\frac{T(x,z,t)-T(x,z-\Delta z,t)}{\Delta z}\right)}{2\Delta z}\right] q(x,z-\Delta z,t) + \left[-\frac{\tilde{s}D_h^*\left(x+\frac{\Delta x}{2},z,t\right)+\tilde{s}D_h^*\left(x-\frac{\Delta x}{2},z,t\right)}{\Delta x^2} - \frac{\tilde{s}D_v^*\left(x,z+\frac{\Delta z}{2},t\right)+\tilde{s}D_v^*\left(x,z-\frac{\Delta z}{2},t\right)}{\Delta z^2} + \right. \tag{S4}$$

$$\left. G\,\frac{\tilde{s}D_{m,v}\left(x,z-\frac{\Delta z}{2},t\right)-\tilde{s}D_{m,v}\left(x,z+\frac{\Delta z}{2},t\right)}{2\Delta z} + \frac{\tilde{s}D_{m,v}\Omega\left(x,z+\frac{\Delta z}{2}\right)\left(\frac{T(x,z+\Delta z,t)-T(x,z,t)}{\Delta z}\right)-\tilde{s}D_{m,v}\Omega\left(x,z-\frac{\Delta z}{2}\right)\left(\frac{T(x,z,t)-T(x,z-\Delta z,t)}{\Delta z}\right)}{2\Delta z}\right] q(x,z,t)\,,$$

with $\mathbf{D}^* \equiv \mathbf{D}_e + \mathbf{D}_m$ a combination of eddy and molecular diffusivity in vertical (D_v^*) and horizontal (D_h^*) direction, Δt time step of integration (s), Δz vertical grid spacing (m), and Δx horizontal grid spacing (m). Here $\tilde{s}, u, w, \Omega, D_h^*, D_v^*, D_{m,v}$ and q are Nx1 vector where N is the number of grid cells; $\mathbf{A}$ and $\mathbf{B}$ are banded square-matrices of dimensions NxN that represent the advection operator (i.e., the sum of the three velocity components) and the diffusion operator (Fickian diffusion, eddy diffusion, thermal diffusion, and gravitational fractionation), respectively. The two matrices have entries on the diagonal as well as four off-diagonals corresponding to the grid points above, below, to the left and to the right. Because $\mathbf{A}$ and $\mathbf{B}$ are also dependent on time, subscripts indicate the time step in Eqs. (S3) and (S4). Equations (S2) – (S4) form a system of linear equations describing the change in time of q at all spatial points. Rearranging Eq. (S2) yields

$$q(x,z,t+\Delta t) = \left[\tilde{s}(z)\,\mathbf{I} - (\mathbf{A}+\mathbf{B})_{|t+\Delta t}\right]^{-1}\left[\frac{\Delta t}{2}(\mathbf{A}+\mathbf{B})_{|t} + \tilde{s}(z)\,\mathbf{I}\right] q(x,z,t)\,, \tag{S5}$$

with $\mathbf{I}$ the identity matrix, which can be stepped forward in time. In the limit of no horizontal transport and constant coefficients ($\tilde{s}, D_m, D_e$ and u constant), we find good agreement between this numerical model and analytical solutions for a simple 1D model (Appendix A, Fig. S2). δ^{15}N profiles from the model run at 5x higher temporal resolution indicate that the error introduced by a coarser time step converges and is small (~0.5 per meg) relative to the signal in the deep firn (~5 per meg) (Fig. S3).
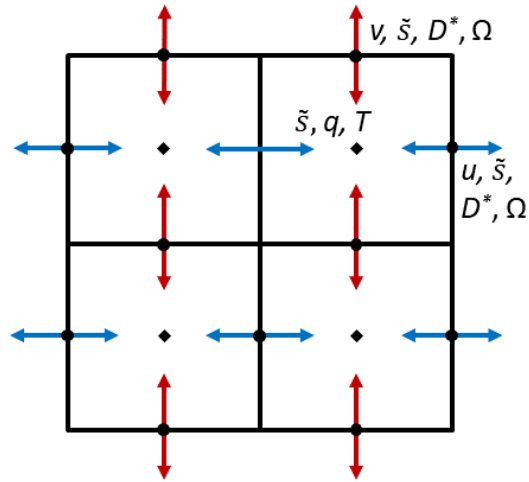
2

Figure S1. Schematic of how variables $q, T, u, \tilde{s}, D^*, \Omega$ and w are defined on the staggered grid.
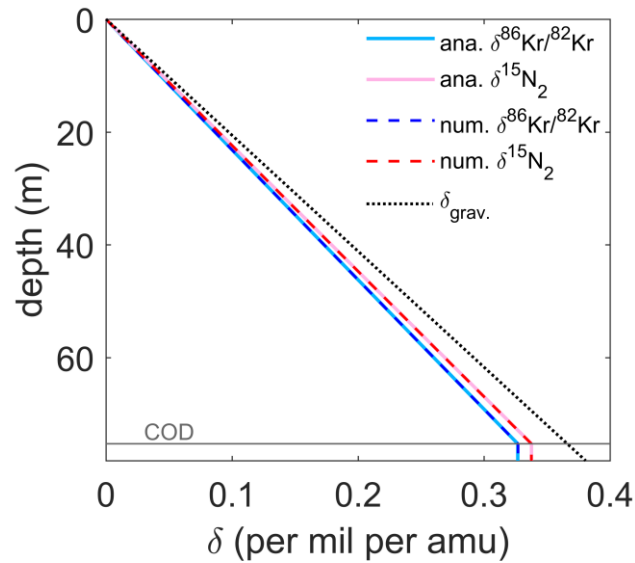

Figure S2. Comparison of 1D analytical solutions (Appendix A, solid lines) and numerical model output (dashed coloured lines). Here $w = 10^{-9}$ m s^{-1}, $D_e = 6 \times 10^{-7}$ m^2 s^{-1} and molecular diffusivity of CO_2 $D_m = 6 \times 10^{-6}$ m^2 s^{-1} up to the COD. The dashed black line shows the gravitational settling equilibrium, i.e., the steady-state solution for each isotope pair neglecting advection and non-fractionating mixing processes (δ_{grav}).

3
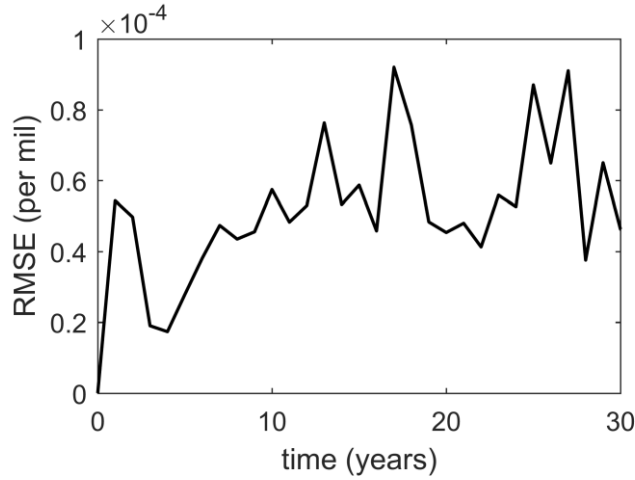
Figure S3. Evolution of the root-mean-square difference between the $\delta^{15}N$ profile produced by the model with barometric pumping and a time step of 3.5 days (default setting) relative to results obtained with 5x higher temporal resolution (assumed to yield the "true" solution). The error is quantified in the depth range of 68-75 m at WAIS Divide and converges at less than 0.1 per meg after ~15 years. The pressure forcing was linearly interpolated for the high-resolution run and the model was initialized with the steady-state solution presented in the main text for both time steps. Interannual variability in the plot is caused by different surface pressures conditions right before each data point was recorded which forced transport of more or less gravitationally fractionated air into the region of interest.

1.2   Layering

We solve the trace gas transport equation under the consideration of discontinuous, impermeable, horizontal layers. Owing to computational limitations, layers are somewhat idealized by assigning them an infinitesimal thickness.

Layers are advected with the firn. The z-axis position of layer l, at time t, is found by numerically integrating the equation

$$z_l(t) = z_l(t_0) + \int_{t_0}^{t} w_{firn}(z_l(t')) \, dt' \, , \tag{S6}$$

from the initial time t_0 where z_l is the depth of the layer and w_{firn} is the vertical firn advection velocity. Equation (S6) is discretized using Forward Euler time stepping such that

$$z_l(t) = z_l(t - \Delta t) + w_{firn}\big(z_l(z - \Delta t)\big)\Delta t \, . \tag{S7}$$

Layer positions on the discrete grid are updated once a layer has moved below the depth of the next grid box. New layers are introduced at 70% of the total depth of the firn column once the top layer was displaced by at least the thickness of one annual layer from its initial position. The centre of each layer opening alternates between two locations (separated by half the horizontal domain length) and the layer size increases linearly with depth. Layers begin to cover the entire horizontal range of the model when the COD is reached and are not tracked further below this depth because any further gas transport is limited to advection with the pores.

1.3   Boundary conditions

A set of boundary and initial conditions accompany Eq. (S1):

4

1) The model is initialized with isotopic ratios as expected from gravitational equilibrium at all depths. For CO_2 and CH_4 transport simulations, initial concentrations are set to the lowest atmospheric concentrations observed for the time window of the simulation.

2) Surface values of q are given by the atmospheric trace gas concentration at each time step (i.e., a Dirichlet boundary). Atmospheric isotope ratios are assumed to be constant. Atmospheric CO_2 and CH_4 histories are taken and updated from Buizert et al. (2012) based on a combination of direct measurements and reconstructions from the Law Dome ice core site (Figure S4) (Etheridge et al., 1996, 1998; Keeling et al., 2001; Dlugokencky et al., 2016a, 2016b).

3) A periodic boundary condition is implemented for all horizontal fluxes.

4) Because Eq. (S1) only describes the trace gas evolution in open pore space, the bottom of the domain is reached where $\tilde{s}$ equals zero. A Neumann boundary condition is chosen for this boundary and the flux leaving through the bottom of the domain is equal to the advection of pores with the firn. Diffusion already ceases to occur at the considerably shallower close-off depth (COD). Because the advective flux at the bottom boundary depends on q, it must be approximated locally using a backward difference scheme.

5) Layers are implemented on the staggered grid by setting the diffusivity and permeability between two adjacent boxes to zero. Layers have an infinitesimally small thickness and do not change the porosity anywhere. The permeability increases from layer edges towards the centre of the layer openings to obtain a more realistic flow field near layer edges. Other firn properties, such as the diffusivity, are changed only on layer grid points because their porosity-dependence should be considerably weaker than for permeability. Vertical gas advection velocities on layers correspond to the local velocity of firn such that mixing ratio discontinuities are preserved and correctly advected downward at the same speed as layers. Layers do not directly impact the horizontal diffusion, permeability or porosity.
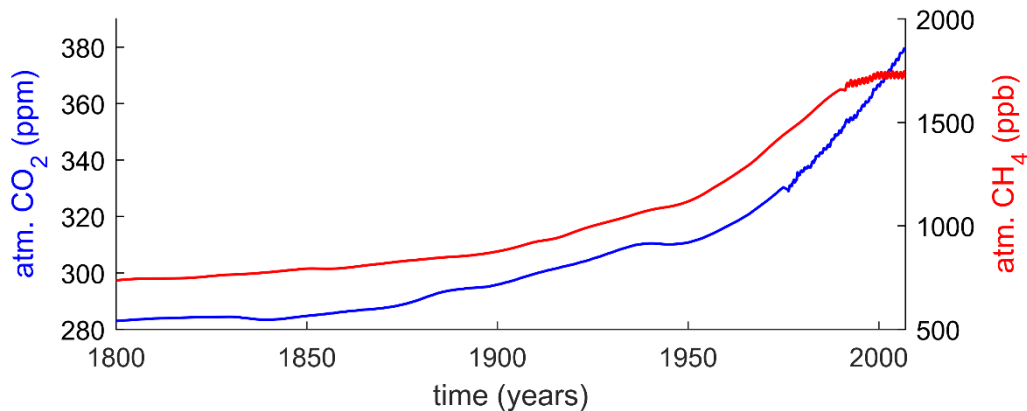

Figure S4. Atmospheric CO_2 and CH_4 histories composed from a combination of direct measurements and reconstructions from the Law Dome ice core site (Etheridge et al., 1996, 1998; Keeling et al., 2001; Buizert et al., 2012; Dlugokencky et al., 2016a, 2016b).

2 Flow field models for firn advection and barometric pumping

2.1 Firn pore advection and pore compression

Advection in the Eulerian frame of the model consist of 3 distinct processes that combine to form the vector $\vec{u}$ in Eq. (S1). The first component of advection represents the downward migration of firn and air contained in the pore spaces due to the continuous accumulation of fresh snow at the surface. This flux can easily be calculated from the snow/ice mass balance and the density profile of the firn. Secondly, the compression of pores in the firn squeezes air out and drives a macroscopic airflow from the firn back to the atmosphere. Finally, barometric pumping drives direction-reversing airflows in response to surface pressure anomalies. These airflows act to return firn air pressures to hydrostatic balance. Barometric pumping flows are orders of magnitude faster than the other fluxes (Fig. 3c) but cause no net airflow when averaged over seasonal or longer time scales. Nevertheless, the fast flow speeds associated with barometric pumping may produce notable dispersive mixing in the deep firn as discussed in the main text (Buizert and Severinghaus, 2016).

The return and barometric pumping flows u_r and u_b move through the porous firn medium and obey Darcy's law. Darcy's law (Darcy, 1856) states that the equilibrium-state volume transport Q through the cross-sectional area A for laminar, incompressible flow is given by

$$Q = -A\frac{\kappa}{\mu}\nabla P, \tag{S8}$$

where κ is permeability of the medium (m²), μ is dynamic viscosity of the fluid (Pa·s), and ∇P is the pressure gradient (Pa m⁻¹) driving the flow. We note that the hydrostatic component of pressure ($\tilde{P}$) is no cause of flow and can thus be removed in the flow field model. We therefore consider only deviatoric pressure $P' \equiv P - \tilde{P}$. Discharge Q must be divided by area A and the pressure-corrected open porosity $\tilde{s}$ to obtain the true flow speed u per pore-cross sectional area used in the tracer advection equation because only a fraction of the total area is available for flow. This results in

$$u = \frac{Q}{A\,\tilde{s}} = -\frac{\kappa}{\mu\,\tilde{s}}\nabla P'. \tag{S9}$$

The continuity equation for a compressible fluid in a porous medium can be derived from the conservation equation of air molecules, using the ideal gas law, which yields

$$\frac{\partial(s_{op}\,\rho)}{\partial t} + \nabla \cdot (s_{op}\,\rho\,u) = s_{op}\,S, \tag{S10}$$

where ρ is air density and S denotes a source or sink of mass (Buizert and Severinghaus, 2016). Assuming porosity is independent of time, $\frac{\partial(s_{op})}{\partial t} = 0$, and the density in the firn is obtained from hydrostatic balance of an isothermal atmosphere, $\rho \simeq \rho_0 \exp\left(\frac{g\,M}{R\,T}\,z\right)$, the continuity equation implies that

6

$$\nabla \cdot (\tilde{s}\,\boldsymbol{u}) = \frac{\tilde{s}\,S}{\rho_0} - \frac{\partial(\rho_0)}{\partial t} \equiv \alpha\,, \tag{S11}$$

where ρ_0 is surface air density, α is a volume source or sink of air. The depth dependency of density has been absorbed into the open porosity as before. Equation (S11) shows that the divergence of the porosity-scaled velocity must equal the local source of air and change in density.

For the return flow of air to the atmosphere (i.e., $\boldsymbol{u}_r$) the source term α_r is the compression of pores during firn advection and density changes are neglected

$$\alpha_r = \nabla \cdot (\tilde{s}\,\boldsymbol{u}_r) = \nabla \cdot \left[-\frac{\kappa}{\mu}\nabla P' \right], \tag{S12}$$

and for the barometric pumping component of flow (i.e., $\boldsymbol{u}_b$) the source or sink α_b is the local density change in response to surface pressure anomalies

$$\alpha_b = \nabla \cdot (\tilde{s}\,\boldsymbol{u}_b) = \nabla \cdot \left[-\frac{\kappa}{\mu}\nabla P' \right]. \tag{S13}$$

α_r can be calculated as the vertical derivative of the mean vertical flow due to pore compression $\langle w_r \rangle = w_{air} - w_{firn}$, where w_{air} is the mean effective vertical air transport velocity (m s^{-1}), such that

$$\alpha_r = \frac{\partial}{\partial z}\left[\tilde{s}\left(w_{air} - w_{firn} \right) \right]. \tag{S14}$$

This is analogous to calculating pore compression in a 1D firn column (Rommelaere et al., 1997). At steady-state, mass conservation of air requires that the net vertical flux of air molecules is equal at all depths when integrated horizontally. Using the ideal gas law, the total vertical transport of air molecules n per area A is given by

$$\frac{n}{A\,t} = \frac{P\frac{V}{t}}{A\,R\,T} = \frac{1}{R\,T}\left(\tilde{P}s_{op}w_{air} + P_b s_{cl}w_{firn} \right) \equiv \text{const.,} \tag{S15}$$

where $\tilde{P}$ is the ambient hydrostatic pressure in open pores, P_b is pressure of air in bubbles, and s_{cl} is closed porosity (m^3 m^{-3}) (Rommelaere et al., 1997). Temporal changes in $\tilde{P}$ are small and their impact on w_{air} and P_b is neglected in Eq. (S15). At $z = z(\text{COD})$, vertical airflow ceases and air is only carried further downward by the advection of pores with the firn. Therefore, w_{air} is equal to the advection velocity at and below this depth and

$$\frac{n}{A\,t} = \frac{1}{R\,T}\left(\tilde{P}s_{op}w_{firn} + P_b s_{cl}w_{firn} \right)_{\big|z=z_{COD}}. \tag{S16}$$

For given bubble pressure P_b, Eqs. (S15) and (S16) can be solved to find w_{air} and α_r at all depths. Rommelaere et al. (1997) derive an equation for the change in bubble air content based on the compression of previously existing bubbles and the trapping of air in new bubbles

$$P_b(z) = \frac{1}{w_{firn}\, s_{cl}} \int_0^z \tilde{P}\, w_{firn} s_t \frac{\partial}{\partial z} \left(\frac{s_{cl}}{s_t}\right) dz\,, \tag{S17}$$

where $s_t \equiv s_{cl} + s_{op}$ is total porosity. Typical pressure profiles are shown in Fig. S5. High P_b near the surface results from the very small, but non-zero closed porosity values that are an artefact of the porosity parameterization at that depth. Mean P_b in the top $\sim$60 % of the firn column above the COD should thus be interpreted with caution.
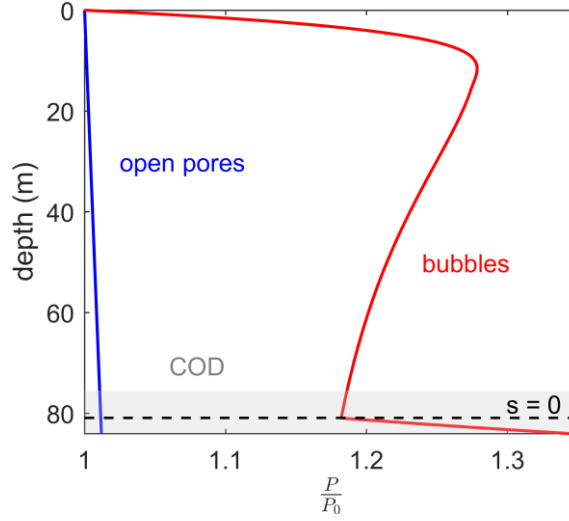
Figure S5. Normalized profiles of pressure in bubbles and of hydrostatic pressure in open pores at WAIS Divide.

Equations (S12), (S14), (S15), and (S17) are combined to calculate the pressure fields for the return flow

$$\frac{\partial}{\partial z}\left[\tilde{s}\left(w_{air} - w_{firn}\right)\right] = \nabla \cdot \left[-\frac{\kappa}{\mu}\nabla P'\right]. \tag{S18}$$

Subsequently, the corresponding velocity field $\boldsymbol{u}_r$ is obtained using Eq. (S9). Plots of a representative pressure anomaly field and corresponding flow field are shown in Figs. S6 and S7.
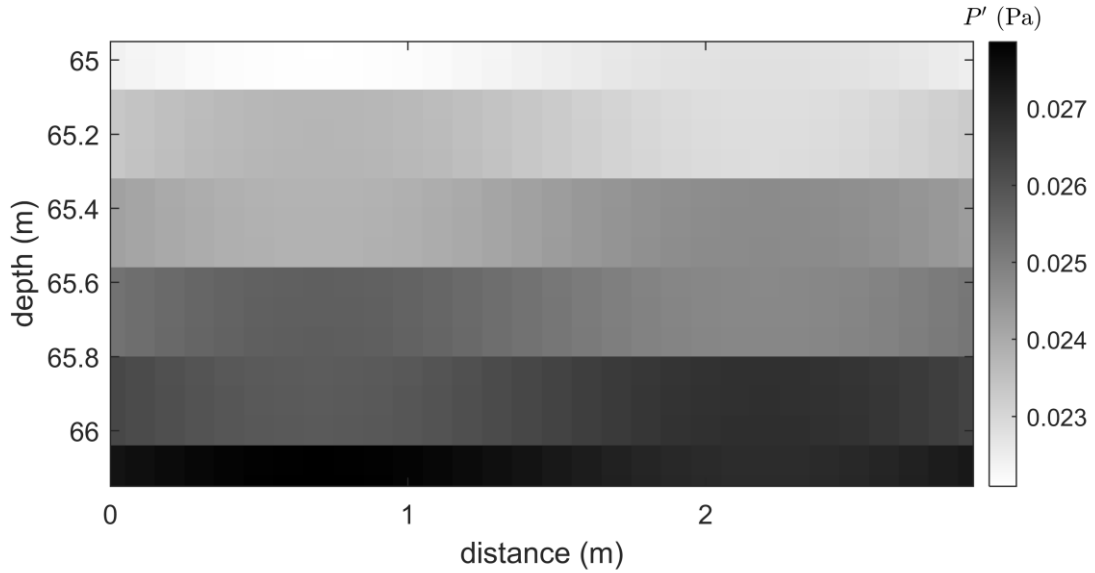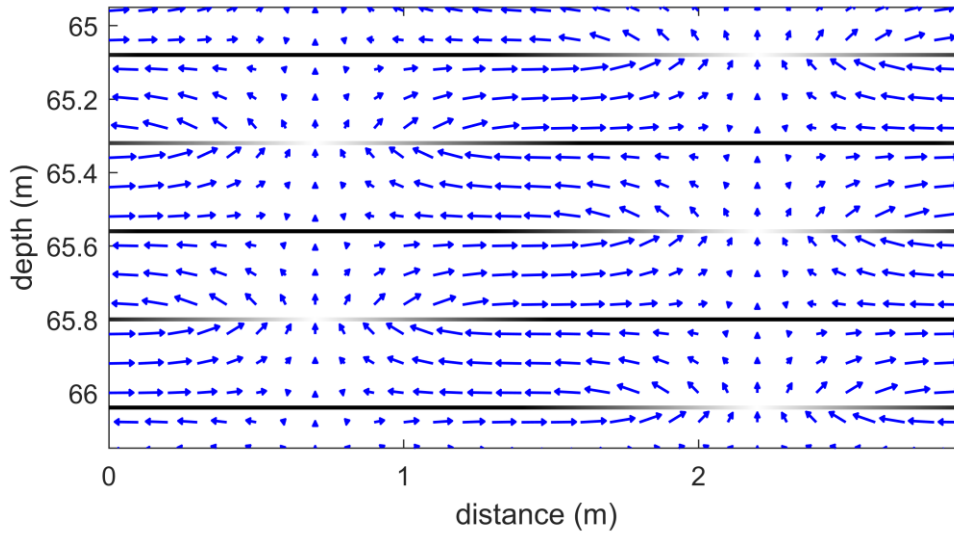
Figure S6. Pressure anomaly field calculated for the return flow to the atmosphere shown in Fig. S7. Layers appear as discontinuities in the pressure field on the model domain. The plot shows a ~1 m section of the deep firn and is presented at reduced grid resolution for clarity.

5 **Figure S7.** Return flow of air to the atmosphere corresponding to Fig. S6. The plot shows a selected region of the deep firn and is presented at reduced grid resolution for clarity. The blackness of layers indicates the local vertical permeability of the firn.

2.2   Barometric pumping

The source term for barometric pumping, α_b, is equal to the change in firn air density caused by surface pressure anomalies associated with passing storms (Fig. S8). Air compression or expansion demands a local convergence or divergence of flow

10 that forces air to move in or out of the firn, assuming porosity remains constant.
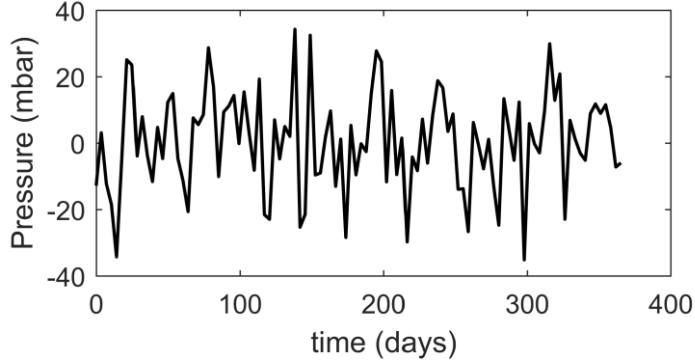
Figure S8. One-year subsection of the surface pressure forcing driving barometric pumping at WAIS Divide. Observed daily pressure variability of ~7 mbar was rescaled by a factor of $\sqrt{\Delta t}$ to account for the longer time step used in the model.

Starting from Darcy's law, the continuity equation and hydrostatic balance, Buizert and Severinghaus (2016) derived a partial differential equation for firn air pressure similar to Eq. (S19)

$$s_{op} \frac{\partial P}{\partial t} = \nabla \cdot \left[s_{op} \, \bar{P}_0 \, \exp\left(\frac{M \, g}{R \, T} z\right) \frac{\kappa}{\tilde{s} \mu} \nabla P' \right]. \tag{S19}$$

Here, we remove the hydrostatic component of pressure through the definition of P' and use the version of Darcy's law given by Eq. (S9). Note that following Buizert and Severinghaus (2016), we linearized Eq. (S19) in the pressure anomaly by replacing the pressure (or equivalently the density) in the continuity equation by the annual mean hydrostatic pressure $\left(P = \bar{P}_0 \exp\left(\frac{M \, g}{R \, T} z\right) \right)$. However, the high computational costs of running a 2D model (~2 days runtime on 10 CPUs per simulation with $\Delta t = 3.5$ days) prevent us from reducing the time step below ~3 days and from explicitly resolving the propagation of surface pressure waves into firn. Instead, we assume that the pressure changes on the LHS are approximately in hydrostatic balance throughout the firn, in line with results by Buizert and Severinghaus (2016):

$$\frac{\partial P}{\partial t} \simeq \frac{\partial \tilde{P}}{\partial t} = \frac{\partial P_0}{\partial t} \exp\left(\frac{M \, g}{R \, T} z\right), \tag{S20}$$

where $P_0 = P_0(t)$ is the time-varying surface pressure. Combining Eqs. (S19) and (S20) yields α_b

$$\alpha_b \equiv \frac{\tilde{s}}{\bar{P}_0} \frac{\partial P_0}{\partial t}, \tag{S21}$$

and an equation to calculate a hypothetical pressure field which gives rise to the barometric pumping flow

$$\frac{\tilde{s}}{\bar{P}_0} \frac{\partial P_0}{\partial t} = \nabla \cdot \left[\frac{\kappa}{\mu} \nabla P' \right], \tag{S22}$$

where $\bar{P}_0$ is the annual mean surface pressure. The flow field, given by Eq. (S9), may be interpreted as the flow required over timestep Δt to return the column to hydrostatic balance with a new surface pressure of P_0. To represent storm activity, we prescribe $P_0(t)$ as pseudo-red noise. The surface pressure variability in the model is slightly damped compared to observations in order to account for non-hydrostatic changes. This yields comparable mean vertical velocities as published by Buizert and

5 Severinghaus (2016).

Similar to Eq. (S1), the flow field models for the return flow and barometric pumping are discretized using central differences on a staggered grid. Values for κ are calculated using the parametrization of Adolph and Albert (2014) and μ is assumed to be constant. Surface values of P' are set to zero for the return flow and to $P_0(t) - \bar{P}_0$ for barometric pumping. The grid is periodic in the x-direction and no fluxes through the bottom boundary are permitted. Layers set the permeability κ, and

10 thus also velocities, between grid boxes to zero. Because layers are advected with the firn, the total flow field must be recalculated at every time step.

3   Thermal model

We use the thermal model of Alley and Koci (1990) to obtain temperature fields for all time steps. The temperature evolution of firn and ice can be simulated in 1D because horizontal temperature gradients are negligibly small. Heat transport in firn is

15 governed by a modified version of the traditional heat equation (Cuffey and Paterson, 2010)

$$\rho c_p \frac{\partial T}{\partial t} = \gamma \frac{\partial^2 T}{\partial z^2} + \frac{\partial \gamma}{\partial z}\frac{\partial T}{\partial z} - \rho c_p w_s \frac{\partial T}{\partial z} + Q \,, \tag{S23}$$

where $T = T(t,z)$ is temperature (°C), $\rho = \rho(z)$ firn density (kg m^{-3}), $c_p = c_p(T)$ specific heat capacity of firn (J kg^{-1} °C^{-1}), $\gamma = \gamma(T,\rho)$ heat conductivity (W m^{-1} °C^{-1}), w_s vertical advection velocity of firn/ice (m s^{-1}), and Q is local heat production due to firn compaction and ice deformation (J s^{-1} m^{-2}). This expression can be rewritten in terms of the thermal diffusivity $k = \frac{\gamma}{c_p \rho}$ as (Johnsen, 1977)

$$\frac{\partial T}{\partial t} = k \frac{\partial^2 T}{\partial z^2} + \left[\left(\frac{k}{\rho} + \frac{\partial k}{\partial \rho}\right)\frac{\partial \rho}{\partial y} - w_s\right]\frac{\partial T}{\partial z} + \left[\frac{\partial k}{\partial T} + \frac{k}{c_p}\frac{dc_p}{dT}\right]\left(\frac{\partial T}{\partial z}\right)^2 + Q \,. \tag{S24}$$

20 Following Alley and Koci (1990), we use the following parametrizations for w_s, c_p and k:

$$w_s = w_{firn}\left(1 - \frac{\sigma}{\rho_{ice}H}\right), \tag{S25}$$

$$c_p = 2096 + 7.7752T \,, \tag{S26}$$

$$k = \left(1 - 0.00882(T + 30)\right)\left(-1.229 \times 10^{-14}\rho^3 + 2.1312 \times 10^{-11}\rho^2 - 9.4 \times 10^{-9}\rho + 1.779 \times 10^{-6}\right), \quad \text{(S27)}$$

where σ is the cumulative load of firn above (kg m^{-2}) and H the total thickness of the ice sheet. Q is parameterized as

$$Q = \sigma\frac{\dot{b}\,\rho_{ice}}{\rho^3}\frac{\partial\rho}{\partial z}\frac{g}{c_p} + \frac{2\left(\frac{\dot{b}}{H}\right)^{\frac{4}{3}}}{\rho\,c_p\left(4.26 \times 10^{-13}\exp\left(-\frac{7217}{T + 273.15}\right)\right)^{\frac{1}{3}}}, \quad \text{(S28)}$$

where $\dot{b}$ is the ice equivalent accumulation rate (m s^{-1}) (Alley and Koci, 1990). Equation (S24) is solved by explicit (forward Euler) time stepping because of the non-linearity in T. Spatial derivatives are approximated by central differences. Since the firn air transport model just requires firn temperature for the last ~200 years, only the top 130 m of the ice sheet are simulated

5 in the temperature model for computational efficiency. The temperature gradient at the bottom boundary is fixed to zero but temperature at that depth can evolve freely. Surface temperature histories for WAIS Divide and Law Dome DSS were previously published by Orsi et al. (2012), Van Ommen et al. (1999) and Dahl-Jensen et al. (1999) and allow us to develop a surface forcing for the model. For the Law Dome site DSSW20K, we combine the water oxygen isotope record translated to temperature following Van Ommen et al. (1999) and supplement this published, six centuries long record with the rescaled

10 mean annual temperature recorded at the nearby Casey Station for the last ~50 years (Jones and Reid, 2001). Further information on the isotope-to-temperature scaling and the relationship to the historic data at Casey station can be found in Van Ommen et al. (1999). An offset is applied to the isotope and instrumental temperatures to match the slightly different mean annual temperature at DSSW20K compared to DSS. The Orsi et al. (2012) best fit WAIS Divide surface temperature record is modified slightly to bring our model results in line with the published borehole temperature profiles (Fig. S9). A site-specific

15 mean seasonal cycle is superimposed on both long-term temperature forcings. The seasonal cycle is generated by matching a sine and cosine wave including several harmonics to a climatology of Automated Weather Station data at WAIS Divide and Law Dome (Lazzara et al., 2012). The exact details of the seasonal cycle are of limited importance for trace gas transport to the lock-in zone because the seasonal temperature wave becomes quickly attenuated in the firn. We do not mean to imply that our forcings are necessarily accurate reconstructions of local surface temperature but the forcings should yield approximately

20 correct thermal gradients in the firn using our model's temperature module. Moreover, thermal fractionation of isotopes only amounts to a comparatively small influence on most isotopes ratios. Thus, an approximately correct temperature profile is sufficient for our purposes. Temperature fields are only used to account for isotope thermal fractionation and any temperature influence on firn densification is neglected.
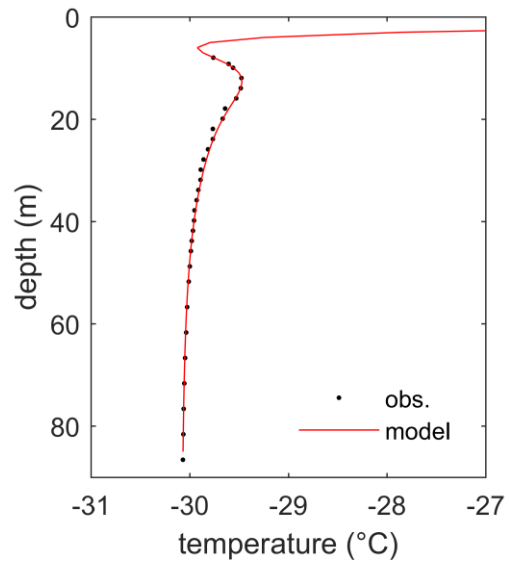
Figure S9. Observed borehole temperature and simulated temperature profile at WAIS Divide in January 2009 (Data from: Orsi et al., 2012).

4 Summary tables

Table S1. Overview of important model parameters

Parameters	WAIS Divide	Law Dome DSSW20K
Firn depth (i.e., open porosity = 0)	85 m	55 m
Model height	80.92 m	52.74 m
Model width	2.85 m (= 12x annual layer thickness)	2.43 m
Horizontal grid spacing	0.03 m	0.03 m
Vertical grid spacing	0.04 m	0.04 m
Depth of occurrence of first layer	56.65 m (= 70 % of firn depth)	36.94 m
Simulation time range & time step	1800–2006 in 3.5-day timesteps	1800–1998.05 in 3.5-day timesteps
Obs. annual mean temperature T[1,2]	243.15 K	253.45 K
Ice sheet thickness H	3500 m	1200 m
Mean surface Pressure [1,2]	789 hPa	850 hPa
Surface pressure variability (1 σ)	7 hPa day^{-1}	11.2 hPa day^{-1}
Ice equiv. advection velocity[1,2]	6.9714×10^{-9} m s^{-1}	5.1706×10^{-9} m s^{-1}
Surface mixed zone eddy diffusion[3] $D_e = D_{e0} \exp\left(-\frac{z}{\tau}\right)$	$D_{e0} = 2.38 \times D_{m0}$ $\tau = 2.5$ m range: $0 - 8$ m $+ 2$ m linear taper	$D_{e0} = 2.4 \times D_{m0}$ $\tau = 3.5$ m range: $0 - 14$ m $+ 2$ m linear taper

[1] WAIS Divide: WAIS Divide Project Members (2016)
[2] Law Dome: Etheridge et al. (1992)
[3] Eq. Kawamura et al. (2013)

Table S2. Overview of selected parameterizations in the model

Density of ice[1]	$\rho_{ice} = 916.5 - 0.14438\,(T - 273.15) - 1.517 \cdot 10^{-4}(T - 273.15)^2$ kg m^{-3}
Free air diffusivities relative to CO$_2$	Table 4 & 5 in SI to Buizert et al. (2012) and references therein
Dispersivity[2] **(assumed isotropic)**	$\alpha(s_{op}) = 1.26 \cdot \exp(-25.7 s_{op})$
Total porosity	$s_t = 1 - \dfrac{\rho_{firn}}{\rho_{ice}}$
Closed porosity[3]	$s_{cl} = 0.37 \cdot s_t \left(\dfrac{s_t}{1 - \frac{831.2}{\rho_{ice}}}\right)^{-7.6}$
Firn density fit $<z_{crit1}$	$\rho_{firn} = a_0 + a_1 z + a_2 \cdot \exp[a_3 \cdot (z_{crit1} - z)]$ kg m^{-3}
$z_{crit1} - z_{crit2}$	$\rho_{firn} = b_0 + b_1 z + b_2 z^2$ kg m^{-3}
$>z_{crit2}$	$\rho_{firn} = \rho_{ice} - \left(\rho_{ice} - \rho(z_{crit2})\right) \cdot \exp\left[-\frac{z - z_{crit2}}{\rho_{ice} - \rho(z_{crit2})}(b_1 + 2 \cdot b_2 z_{crit2})\right]$ kg m^{-3}

	WAIS Divide	**Law Dome DSSW20K**
Density fit parameters[4]	$z_{crit1} = 16$	$z_{crit1} = 19.7186$
	$z_{crit2} = 110$	$z_{crit2} = 37.4193$
	$a_0 = 420$	$a_0 = 511.8111$
	$a_1 = 20.0121$	$a_1 = 7.8210$
	$a_2 = -151.242$	$a_2 = -0.0476$
	$a_3 = -0.1$	$a_3 = 0.4143$
	$b_0 = 506.85$	$b_0 = 556.5176$
	$b_1 = 5.3748$	$b_1 = 5.3204$
	$b_2 = -0.0152$	$b_2 = 0.0117$

[1] Eq: Schwander et al. (1997)
[2] original Eq: Buizert and Severinghaus (2016)
[3] Eq: Goujon et al. (2003) in Severinghaus et al. (2010) and Kawamura et al. (2013)
[4] data: Trudinger et al. (1997); WAIS Divide coefficients: Battle et al. (2011)
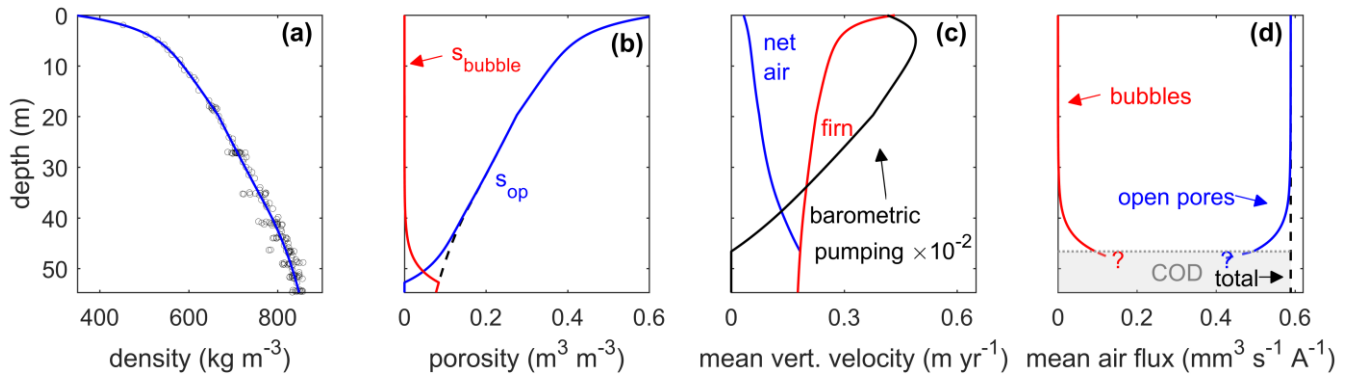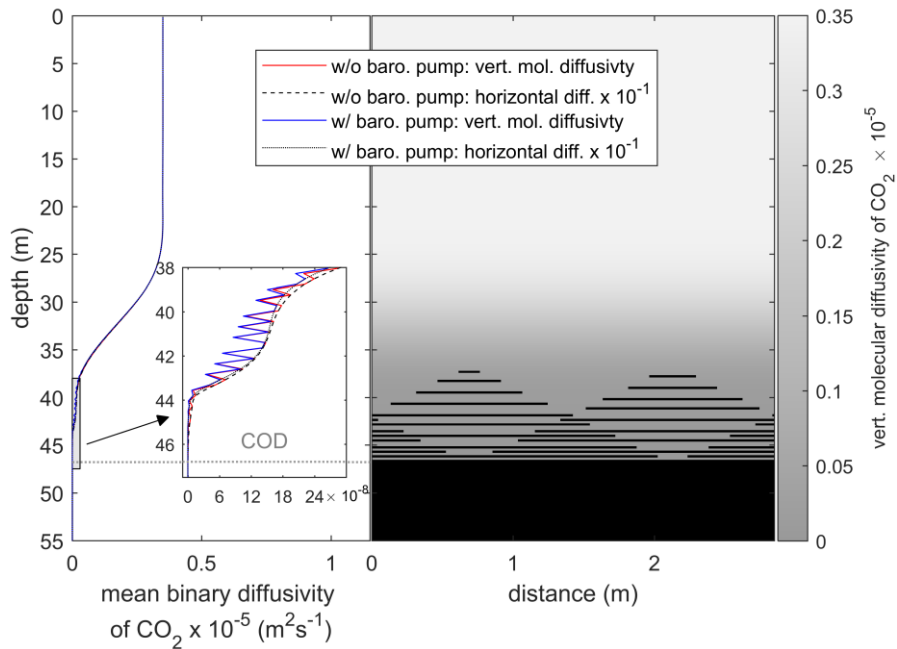
5 Law Dome DSSW20K firn properties

Figure S10. Same as Fig. 3 for Law Dome DSSW20K. Density data: Trudinger et al. (2002, 2013)

Figure S11. Same as Fig. 5 for Law Dome DSSW20K. Every third annual layer is shown.
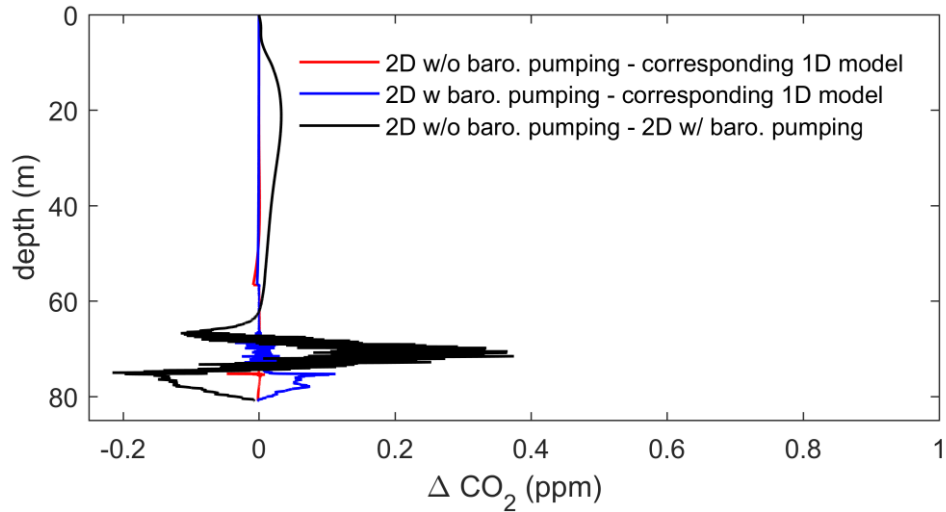
6 Mass normalization

Isotope ratios in delta notation are mass-normalized to an isotope mass difference of one atomic mass unit (amu) using q-values

$$q_{norm} = q^{\frac{1}{1000 \times \Delta m}}.$$

This is more accurate than dividing the ratio in delta notation by the isotope mass difference in amu (e.g. divide $\delta^{40}Ar/^{36}Ar$ by ~4 amu).

7   Additional supporting Figures

Figure S12. Comparison of simulated CO_2 values at WAIS Divide between both 2D models (black line) and between each 2D model and the corresponding 1D model (red and blue line).
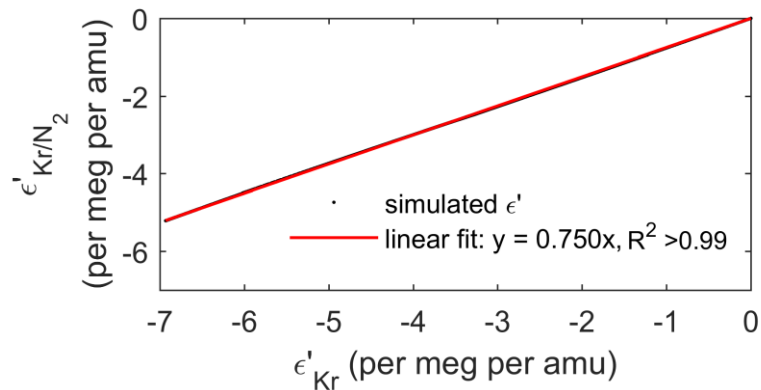

Figure S13. Linear fit to the relationship between mass-normalized ϵ' of $^{84}Kr/^{28}N_2$ and ϵ' of $^{86}Kr/^{82}Kr$ observed in the 2D model with barometric pumping at WAIS Divide.

8   References

Adolph, A. C. and Albert, M. R.: Gas diffusivity and permeability through the firn column at Summit, Greenland: Measurements and comparison to microstructural properties, Cryosphere, 8(1), 319–328, doi:10.5194/tc-8-319-2014, 2014.

Alley, R. B. and Koci, B. R.: Recent warming in central Greenland?, Annals of Glaciology, 14, 6–8, 1990.

5   Battle, M. O., Severinghaus, J. P., Sofen, E. D., Plotkin, D., Orsi, A. J., Aydin, M., Montzka, S. A., Sowers, T. and Tans, P. P.: Controls on the movement and composition of firn air at the West Antarctic Ice Sheet Divide, Atmospheric Chemistry and Physics, 11, 11007–11021, doi:10.5194/acp-11-11007-2011, 2011.

Buizert, C. and Severinghaus, J. P.: Dispersion in deep polar firn driven by synoptic-scale surface pressure variability, The Cryosphere, 10, 2099–2111, doi:10.5194/tc-2016-148, 2016.

10   Buizert, C., Martinerie, P., Petrenko, V. V., Severinghaus, J. P., Trudinger, C. M., Witrant, E., Rosen, J. L., Orsi, A. J., Rubino, M., Etheridge, D. M., Steele, L. P., Hogan, C., Laube, J. C., Sturges, W. T., Levchenko, V. A., Smith, A. M., Levin, I., Conway, T. J., Dlugokencky, E. J., Lang, P. M., Kawamura, K., Jenk, T. M., White, J. W. C., Sowers, T., Schwander, J. and Blunier, T.: Gas transport in firn: Multiple-tracer characterisation and model intercomparison for NEEM, Northern Greenland, Atmospheric Chemistry and Physics, 12, 4259–4277, doi:10.5194/acp-12-4259-2012, 2012.

15   Cuffey, K. M. and Paterson, W. S. B.: The Physics of Glaciers, 4th ed., Butterworth-Heinemann/Elsevier, Burlington, MA., 2010.

Dahl-Jensen, D., Morgan, V. I. and Elcheikh, A.: Monte Carlo inverse modelling of the Law Dome (Antarctica) temperature profile, Annals of Glaciology, 29, 145–150, doi:10.3189/172756499781821102, 1999.

Darcy, H.: Les Fontaines Publiques de la Ville de Dijon, Victor Dalmont, Paris., 1856.

20   Dlugokencky, E. J., Lang, P. M., Mund, J. W., Crotwell, A. M., Crotwell, M. J. and Thoning, K. W.: Atmospheric Carbon Dioxide Dry Air Mole Fractions from the NOAA ESRL Carbon Cycle Cooperative Global Air Sampling Network, 1968-2015, Version: 2016-08-30, 2016a.

Dlugokencky, E. J., Lang, P. M., Crotwell, A. M., Mund, J. W., Crotwell, M. J. and Thoning, K. W.: Atmospheric Methane Dry Air Mole Fractions from the NOAA ESRL Carbon Cycle Cooperative Global Air Sampling Network, 1983-2015, Version: 25   2016-07-07, 2016b.

Etheridge, D. M., Pearman, G. I. and Fraser, P. J.: Changes in tropospheric methane between 1841 and 1978 from a high accumulation-rate Antarctic ice core, Tellus, 44B, 282–294, doi:10.1034/j.1600-0889.1992.t01-3-00006.x, 1992.

Etheridge, D. M., Steele, L. P., Langenfelds, R. L., Francey, R. J., Barnola, J. M. and Morgan, V. I.: Natural and anthropogenic changes in atmospheric CO2 over the last 1000 years from air in Antarctic ice and firn, Journal of Geophysical 30   Research-Atmospheres, 101(D2), 4115–4128, doi:10.1029/95JD03410, 1996.

Etheridge, D. M., Steele, L. P., Francey, R. J. and Langenfelds, R. L.: Atmospheric methane between 1000 A.D. and present: Evidence of anthropogenic emissions and climatic variability, Journal of Geophysical Research, 103(D13), 15979, doi:10.1029/98JD00923, 1998.

17

Goujon, C., Barnola, J.-M. and Ritz, C.: Modeling the densification of polar firn including heat diffusion: Application to close-off characteristics and gas isotopic fractionation for Antarctica and Greenland sites, Journal of Geophysical Research, 108, 4792, doi:10.1029/2002JD003319, 2003.

Johnsen, S. J.: Stable isotope profiles compared with temperature profiles in firn with historical temperature records, Isotopes and Impurities in Snow and Ice, 388–392, 1977.

Jones, P. D. and Reid, P. A.: A databank of Antarctic surface temperature and pressure data, ORNL/CDIAC-27, NDP-032, Carbon Dioxide Information Analysis Center, Oak Ridge National Laboratory, U.S. Department of Energy, Oak Ridge, Tennessee., 2001.

Kawamura, K., Severinghaus, J. P., Albert, M. R., Courville, Z. R., Fahnestock, M. A., Scambos, T. A., Shields, E. and Shuman, C. A.: Kinetic fractionation of gases by deep air convection in polar firn, Atmospheric Chemistry and Physics, 13, 11141–11155, doi:10.5194/acp-13-11141-2013, 2013.

Keeling, C. D., Stephen, C., Piper, S. C., Bacastow, R. B., Wahlen, M., Whorf, T. P., Heimann, M. and Meijer, H. A.: Exchanges of atmospheric CO_2 and $^{13}CO_2$ with the terrestrial biosphere and oceans from 1978 to 2000., Global Aspects, SIO Reference Series. Scripps Institution of Oceangraphy, San Diego, 01–06, 83–113, doi:10.1007/b138533, 2001.

Lazzara, M. A., Weidner, G. A., Keller, L. M., Thom, J. E. and Cassano, J. J.: Antarctic automatic weather station program: 30 years of polar observations, Bulletin of the American Meteorological Society, 93, 1519–1537, doi:10.1175/BAMS-D-11-00015.1, 2012.

Van Ommen, T. D., Morgan, V. I., Jacka, T. H., Woon, S. and Elcheikh, A.: Near-surface temperatures in the Dome Summit South (Law Dome, East Antarctica) borehole, Annals of Glaciology, 29, 141–144, doi:doi:10.3189/172756499781821382, 1999.

Orsi, A. J., Cornuelle, B. D. and Severinghaus, J. P.: Little Ice Age cold interval in West Antarctica: Evidence from borehole temperature at the West Antarctic Ice Sheet (WAIS) Divide, Geophysical Research Letters, 39(L09710), 1–7, doi:10.1029/2012GL051260, 2012.

Rommelaere, V., Arnaud, L. and Barnola, J.-M.: Reconstructing recent atmospheric trace gas concentrations from polar firn and bubbly ice data by inverse methods, Journal of Geophysical Research, 102(D25), 30069–30083, 1997.

Schwander, J., Sowers, T., Barnola, J. M., Blunier, T., Fuchs, A. and Malaizé, B.: Age scale of the air in the summit ice: Implication for glacial-interglacial temperature change, Journal of Geophysical Research, 102(D16), 19483–19493, doi:10.1029/97JD01309, 1997.

Severinghaus, J. P., Albert, M. R., Courville, Z. R., Fahnestock, M. A., Kawamura, K., Montzka, S. A., Mühle, J., Scambos, T. A., Shields, E., Shuman, C. A., Suwa, M., Tans, P. and Weiss, R. F.: Deep air convection in the firn at a zero-accumulation site, central Antarctica, Earth and Planetary Science Letters, 293, 359–367, doi:10.1016/j.epsl.2010.03.003, 2010.

Trudinger, C. M., Enting, I. G., Etheridge, D. M., Francey, R. J., Levchenko, V. A., Steele, L. P., Raynaud, D. and Arnaud, L.: Modeling air movement and bubble trapping in firn, Journal of Geophysical Research: Atmospheres, 102(D6), 6747–6763, doi:10.1029/96JD03382, 1997.

Trudinger, C. M., Etheridge, D. M., Rayner, P. J., Enting, I. G., Sturrock, G. A. and Langenfelds, R. L.: Reconstructing atmospheric histories from measurements of air composition in firn, Journal of Geophysical Research Atmospheres, 107(24), 1–13, doi:10.1029/2002JD002545, 2002.

Trudinger, C. M., Enting, I. G., Rayner, P. J., Etheridge, D. M., Buizert, C., Rubino, M., Krummel, P. B. and Blunier, T.:
5   How well do different tracers constrain the firn diffusivity profile?, Atmospheric Chemistry and Physics, 13, 1485–1510, doi:10.5194/acp-13-1485-2013, 2013.

WAIS Divide Project Members: WAIS Divide Site Characteristics, [online] Available from: http://www.waisdivide.unh.edu (Accessed 15 November 2016), 2016.